Regional Primitive Equation Studies of the Gulf Stream Meander and Ring Formation Region

MICHAEL A. SPALL* AND ALLAN R. ROBINSON

Division of Applied Sciences, Harvard University, Cambridge, Massachusetts

(Manuscript received 16 December 1988, in final form 12 September 1989)

ABSTRACT

Primitive equation and quasi-geostrophic eddy resolving, open ocean models are used for hindcast studies in the Gulf Stream meander and ring formation region. A feature model approach is used to initialize the models, based on one month of observations during November to December 1984. Flat bottom and topographic calculations are carried out using an initial Gulf Stream velocity profile based on the Pegasus dataset. All of the major events observed in the upper thermocline are reproduced by both numerical models. The addition of bottom topography is shown to significantly alter the character of the deep velocity fields. Large, basin scale circulations found near the bottom in both flat bottom calculations were replaced by energetic jets and eddies associated with the dominant spatial scales of the bottom topography. Use of the quasi-geostrophic model to dynamically adjust the initial conditions for the primitive equation model is shown to reduce the growth of large scale meanders on time scales of one month. A local primitive equation energy and vorticity analysis (PRE-EVA) routine is used to determine the dominant processes of simulated warm and cold ring formation events. The warm ring formation is achieved by differential horizontal advection of a developed meander system. The cold ring formation involves geostrophic and ageostrophic horizontal advection, vertical advection, and baroclinic conversion. Ageostrophic horizontal and vertical advections and stronger baroclinic conversion are believed to be responsible for the more realistic structure of the rings produced by the primitive equation model.

1. Introduction

The region of the Gulf Stream between Cape Hatteras and the Grand Banks is one of the most interesting and challenging places for oceanographic study. The currents are strong and highly variable with spatial scales of tens to thousands of kilometers and temporal scales ranging from days to months. Phenomena of interest include Gulf Stream meanders, warm and cold ring formations, ring–ring and ring–stream interactions, warm outbreaks, mesoscale eddy generation, as well as deep countercurrents and recirculations. The Gulf Stream Meander and Ring system (GSM&R) also has implications in other fields of study such as and air–sea interaction and climate, biological activity, and chemical processes. The GSM&R has important commercial consequences as well in terms of ocean shipping, fisheries, resource exploration, and waste disposal. Understanding and predicting the four-dimensional variability of this complex current system will significantly impact the future of these efforts.

Process and regional ocean models have been used to study the dynamics and energetics of the Gulf Stream system since the early 1980s and are contributing to the understanding of the local dynamics, role of bottom topography, and the processes of ring formations. Idealized meander growth experiments in a periodic channel were carried out with quasi-geostrophic physics by Ikeda (1981) and Ikeda and Apel (1981). The influence of bottom topography on the long term statistics of Gulf Stream meander and ring formation events was investigated by Hurlburt and Thompson (1984) and Adamec (1988). A contour dynamics approach was used by Pratt and Stern (1986) in the study of warm ring formation events. Robinson et al. (1989, hereafter RSP) introduced a regional open ocean quasi-geostrophic model for hindcasting and forecasting observed Gulf Stream events via real data initialization in terms of feature models. Subsequently, EVA, a local Energy and Vorticity Analysis scheme, was used for diagnosis of warm and cold ring formation events.

In this paper, primitive equation and quasi-geostrophic open ocean models are used for hindcast experiments and the analysis of cold and warm ring formation events. The objectives of this research are to study: the differences in PE and QG physics; PE vorticity and energy balances; influence of bottom topog-

* Current address: National Center for Atmospheric Research Boulder, Colorado.

Corresponding author address: Dr. Allan R. Robinson, Harvard University, Division of Applied Sciences, Pierce Hall, Cambridge, MA 02138.

raphy on one month time scales; under what circumstances quasi-geostrophy can function over high topography; and the ability to hindcast Gulf Stream meander and ring formation events with a regional primitive equation model. The models are initialized with and compared to one month of observations from November to December 1984, the same dataset used by RSP. This period was chosen because the relatively good satellite coverage indicated the occurrence of several dynamical events including warm and cold ring formations, ring absorptions, and meander propagation and evolution. The feature model initialization technique introduced by RSP is used for initialization of the numerical models. Feature models are analytical representations of identifiable current structures based on historical data. A PRimitive Equation Energy and Vorticity Analysis scheme (PRE-EVA) is used to study the dominant physical processes of simulated warm and cold ring formation events.

The dynamical models and energy and vorticity analysis package used in this study are reviewed in section 2. The feature models and initialization methodology are summarized in section 3. The SST data and regions of interest for the hindcast study are discussed in section 4. In section 5 the PE and QG bottom topography experiments are carried out and discussed. The effects of using an initial condition for the PE model, which has been partially spun up with the QG model, is investigated in section 6. PRE-EVA analysis of warm and cold ring formation events are presented in section 7. Conclusions from this study are given in section 8.

2. Numerical models and analysis package

In this section, the numerical models and primitive equation analysis package are reviewed. Details of the primitive equation model and its application to open ocean flows may be found in Spall and Robinson (1989, hereafter SR). The quasi-geostrophic model is documented for open ocean flows by Miller et al. (1981) and Robinson and Walstad (1987); its application to the Gulf Stream region is described by RSP. The PRimitive Equation Energy and Vorticity Analysis (PRE-EVA) package and methodology is described in detail by Spall (1989).

a. The primitive equation model

The primitive equation model used in this study has open ocean boundary conditions in the horizontal and hybrid coordinates in the vertical. The primitive equations assume that the fluid is hydrostatic and that the Boussinesq approximation is valid. Hybrid coordinates involve a simple transformation of variables in the vertical for all model levels below a prescribed depth z_c:

$$\sigma(x, y, x) = \frac{z - z_c}{H'} \tag{1}$$

where

$$H' = H(x, y) - z_c, \quad z_c \leqslant z \leqslant H(x, y). \tag{2}$$

In this way the model surfaces follow the topography $[H(x, y)]$ smoothly over the entire domain below z_c, all levels shallower than z_c remain horizontal. The vertical resolution below z_c is increased in shallow regions such as over seamounts or along a coast. Because the surfaces on which the prognostic variables are calculated are no longer horizontal, cross terms appear in the equations of motion. The sigma coordinate vertical velocity is defined as

$$\omega = \frac{1}{H'}[w - \sigma(uH'_x + vH'_y)]. \tag{3}$$

Application of the conservation of momentum gives the x, y, and z momentum equations, written below in hybrid coordinates:

$$u_t + \frac{1}{H'}(H'uu)_x + \frac{1}{H'}(H'vu)_y + (u\omega)_\sigma - fv = -\frac{1}{\rho_0}(P_x - g\sigma H'_x\rho) + F_{mh} + F_{mz} \tag{4}$$

$$v_t + \frac{1}{H'}(H'uv)_x + \frac{1}{H'}(H'vv)_y + (v\omega)_\sigma + fu = -\frac{1}{\rho_0}(P_y - g\sigma H'_y\rho) + F_{mh} + F_{mz} \tag{5}$$

$$P = H'g\int_0^\sigma \rho d\sigma \tag{6}$$

where u, v, and ω are the velocities in the zonal, meridional, and sigma coordinate directions, respectively; Ω is the rotation rate of the earth and ϕ is the latitude. The F_{mh} and F_{mz} are parameterizations of the horizontal and vertical viscous forces, P is the pressure, ρ is the density, and g is the gravitational acceleration.

Conservation of mass for an incompressible fluid is used to derive the continuity equation.

$$\frac{1}{H'}(H'u)_x + \frac{1}{H'}(H'v)_y + \omega_\sigma = 0. \tag{7}$$

The energy equation without sources or sinks may be written in terms of the temperature (T) and salinity (S) as

$$T_t + \frac{1}{H'}(H'uT)_x + \frac{1}{H'}(H'vT)_y + (\omega T)_\sigma = F_{hh} + F_{hz} \tag{8}$$

$$S_t + \frac{1}{H'}(H'uS)_x + \frac{1}{H'}(H'vS)_y + (\omega S)_\sigma = F_{hh} + F_{hz}. \tag{9}$$

An equation of state is used to close the system.

$$\rho = \rho(T, S, P) \tag{10}$$

For levels above the transformation depth, these equations are valid with $H' = z_c$ and the standard primitive equations are recovered.

The numerical model solves equations (4), (5), (6), (7), (8), (9), and (10) subject to initial and boundary conditions. The vertical boundary conditions are a rigid lid at the surface and no normal flow through the bottom.

$$w = 0, \quad z = 0 \tag{11}$$

$$w = uH_x + vH_y, \quad z = H(x, y). \tag{12}$$

The horizontal open boundary conditions are analogous to the Charney, Fjortoft and Von Neumann boundary conditions first proposed for the quasi-geostrophic equations (Charney et al. 1950). The density and normal velocity are specified on all horizontal boundary points and the tangential velocity is specified on inflow points only. On outflow, two dimensional vorticity equations are solved for the vertical vorticity and the barotropic vertical vorticity. The finite difference form of vorticity is then inverted to obtain the tangential velocity. The vorticity equations and calibration of the boundary conditions are discussed by SR.

A Shapiro filter has been used for the horizontal subgridscale parameterization in each of the experiments in this paper. This filter is a highly scale selective smoothing operation originally developed for meteorological applications (Shapiro 1970); its use in ocean modeling is documented by Robinson and Walstad (1987) and SR. For sloping surfaces, depths below z_c, the filter operation has been projected onto horizontal surfaces as described by SR.

b. *The quasi-geostrophic model*

The Harvard quasi-geostrophic open ocean model (Miller et al. 1981) solves the following nondimensional form of the potential vorticity equation

$$\frac{\partial}{\partial t}(\nabla^2\psi + \Gamma^2(\sigma\psi_z)_z) + \alpha J(\psi, \nabla^2\psi) + \alpha\Gamma^2 J(\psi, (\sigma\psi_z)_z) + \beta\psi_x = F_{pqr} \tag{13}$$

where ψ is the geostrophic streamfunction field, J the Jacobian operator, and

$$\alpha = t_0\frac{V_0}{d}, \quad \beta = t_0\beta_0 d,$$

$$\Gamma^2 = \frac{f_0^2 d^2}{N_0^2 H_0^2}, \quad \sigma = \frac{N_0^2}{N^2(z)}.$$

The numerical solution procedure uses finite elements in the horizontal and finite differences in the vertical. Here F_{prq} is the symbolic representation of a Shapiro filter operation on the vorticity field, a filter of order p is applied q times every r time steps. Use of the Shapiro filter as a parameterization of subgrid scale processes has been documented for quasi-geostrophic open ocean flows by Robinson and Walstad (1987). f_o is the Coriolis parameter at the center of the model domain, β_0 is the variation of f with latitude, $N^2(z)$ is the Brunt–Väisälä frequency, and N_0^2 is the Brunt–Väisälä frequency at mid-thermocline. t_0, V_0, d and H_0 are the nondimensional time, velocity, horizontal and vertical length scales, respectively.

The implementation of topography in the QG model is accomplished through the vertical velocity imposed in the bottom boundary condition. The vertical velocity is calculated by a no normal flow condition at the mean bottom depth as

$$w = -v\cdot\nabla H. \tag{14}$$

The gradient of the bottom topography is calculated directly from the actual depth but it is treated as though it was at the mean bottom depth. This approximation is good for bottom topography that is not very tall and does not have a steep slope. Tall topography uses the wrong horizontal velocity and imposes the vertical velocity at the wrong depth. In addition, this may result in flow at model levels that go through the physical bottom. In the case of steep topography, the vertical velocity calculated by Eq. (14) may exceed that which is allowed in the QG approximation if the flow is across, rather than along, the topographic slope. The maximum allowable vertical velocity is derived from the continuity equation as

$$w_{\max} = \epsilon\frac{V_0 H_0}{d} = \frac{V_0^2 H_0}{f_0 d^2}. \tag{15}$$

The vertical advection of relative vorticity, the vertical advection of the perturbation density, and the twisting terms, which are included in the primitive equations, are neglected in the quasi-geostrophic approximation. In the event that the vertical velocity becomes larger than what was assumed in the derivation of the quasi-geostrophic equations, these neglected terms may become important. The vertical velocity, which is imposed at the bottom in the quasi-geostrophic calculation with topography, will be calculated and discussed in section 5c. It is important to recognize the sources of potential error and the limitations of the topography in the QG model but that useful results may nonetheless be obtained.

c. *The PRE-EVA analysis package*

PRE-EVA is a PRimitive Equation Energy and Vorticity Analysis package to be used with the output of the primitive equation model described in section 2a. It solves the vorticity and divergence form of the horizontal momentum equations and the kinetic and available gravitational energy equations.

The velocity field is first decomposed into the ro-

tational and irrotational components via the streamfunction ψ and velocity potential χ:

$$\mathbf{v} = \mathbf{k} \times \nabla\psi + \nabla\chi. \tag{16}$$

This leads to the variables relative vorticity, ζ, and horizontal divergence, D:

$$\zeta = \nabla^2\psi, \quad D = \nabla^2\chi. \tag{17}$$

The streamfunction discussed in this section represents the rotational component of the full primitive equation velocity field and should not be confused with the quasi-geostrophic streamfunction in Eq. (13).

The vertical vorticity equation is derived from the horizontal momentum equations by cross differentiating and summing to eliminate the pressure term. Substituting for the streamfunction and velocity potential, the final vorticity equation is written below (Bateen 1984), valid for depths above z_c. The equation is also written in symbolic form for future discussion.

$$[\zeta_t]^{qg} = -[J(\psi, \zeta)]^{qg} - [J(\psi, f)]^{qg} - [f\nabla^2\chi]^{qg} - [\nabla\chi\cdot\nabla f]^{lb} - [\nabla\chi\cdot\nabla\zeta]^{fb} - [\zeta\nabla^2\chi]^{fb} - [w\zeta_z]^{fb} - [\nabla w\cdot\nabla\psi_z]^{fb} - J(w, \chi_z) + [B\zeta_{zz}]^{qg} + [F_h]^{qg} \tag{18}$$

$$\dot{R} = -\Delta_0 F_R - \Delta_0 F_P - fD - \Delta_1 F_P - \Delta_1 F_R - RD - \delta f_R - \delta\xi_0 - \delta\xi_1 + F_z + F. \tag{19}$$

Each term in the original equation has been given a superscript according to the order to which it is retained in the consistent expansion from quasi-geostrophic to primitive equation physics (Lorenz 1960). The superscript $[\cdot]^{qg}$ indicates that only those terms are retained in the quasi-geostrophic approximation; $[\cdot]^{lb}$ are the additional terms retained for the linear balance equations; the $[\cdot]^{fb}$ terms are also included for the full balance equations; and all of the terms are included for the full primitive equations. A scaling analysis is used to derive these and other sets of equations intermediate in physics between primitive equation and quasi-geostrophy by Gent and McWilliams (1983).

To derive the horizontal divergence equation, the momentum equations are operated on with the vector operator $\nabla\cdot(\ )$ and added. The final form is given below, with the appropriate superscripts as defined for the vorticity equation.

$$D_t = -[\nabla^2(P/\rho_0)]^{qg} + [f\nabla^2\psi]^{qg} + [\nabla f\cdot\nabla\psi]^{lb} - J(f, \chi) - \{\nabla\cdot[(\mathbf{k}\times\nabla\psi)\cdot\nabla(\mathbf{k}\times\nabla\psi)]\}^{fb} - \nabla\cdot[(\mathbf{k}\times\nabla\psi)\cdot\nabla^2\chi] - \nabla\cdot[\nabla\chi\cdot\nabla(\mathbf{k}\times\nabla\psi)] - \nabla\cdot(\nabla\chi\cdot\nabla^2\chi) - \nabla w\cdot(\mathbf{k}\times\nabla\psi)_z - \nabla w\cdot\nabla\chi_z + [BD_{zz}]^{qg} + [F_h]^{qg} \tag{20}$$

$$\dot{D} = -D_2 P + fR - \Delta_0 D_P - \Delta_1 D_P - \Delta_0\Delta_0 - \Delta_0\Delta_1 - \Delta_1\Delta_0 - \Delta_1\Delta_1 - \delta\Delta_0 - \delta\Delta_1 + F_z + F. \tag{21}$$

The kinetic energy equation is derived by multiplying the x, y, and z momentum equations by u, v, and w, respectively, and then summing. The final kinetic energy equation is written below where $K = \frac{1}{2}(u^2 + v^2)^{1/2}$. Because $w \ll u, v$ it is dropped from the definition of K.

$$\frac{\partial K}{\partial t} = -[\nabla\cdot(\mathbf{u}_0 K)]^{qg} - [\nabla\cdot(\mathbf{u}_1 K)]^{fb} - (wK)_z - \left[\nabla\cdot\left(\frac{p}{\rho_0}\mathbf{u}\right)\right]^{qg} - \left[\left(\frac{p}{\rho_0}w\right)_z\right]^{qg} + [g\Delta w]^{qg} - [AK_{zz}]^{qg} + [F]^{qg} \tag{22}$$

$$\dot{K} = -\Delta F_K - \delta f_K - \Delta F_\pi - \delta f_\pi + b - F_z + F_h. \tag{23}$$

To obtain the available gravitational energy equation, the prognostic equation for density (analogous to Eq. 8 but for ρ) is multiplied by $-(\rho_0 g\Delta)/(\partial\tilde{p}/\partial z)$, where $\Delta = \rho(x, y, z) - \tilde{\rho}(z)$. The available gravitational energy is defined as $A = g\Delta^2/[2(\partial\tilde{p}/\partial z)]$. When derived in this fashion, the buoyancy conversion term (b) between kinetic energy and available gravitational energy is equal and opposite in both equations. The horizontal advections have been split into their geostrophic ($\mathbf{u}_0$) and ageostrophic ($\mathbf{u}_1$) components.

$$\left[\frac{\partial A}{\partial t}\right]^{qg} = -[\nabla\cdot(\mathbf{u}_0 A)]^{qg} - [\nabla\cdot(\mathbf{u}_1 A)]^{lb} - [(wA)_z]^{lb} - \left[\frac{A}{2s}w\frac{\partial s}{\partial z}\right]^{lb} - [g\Delta w]^{qg} - [A_h A_{zz}]^{qg} + [F]^{qg} \tag{24}$$

where $s = \partial\tilde{p}/\partial z$.

$$\dot{A} = -\Delta_0 F_A - \Delta_1 F_A - \delta f_A - \delta\bar{\rho} - b - F_z + F_h. \tag{25}$$

3. Feature model initialization

The methodology of using feature models to initialize the quasi-geostrophic model was introduced by RSP. To summarize, the feature model initialization methodology utilizes: (*i*) any available data to locate the surface fronts associated with the positions of the stream axis and of any rings that may be present; (*ii*) feature models based on previous subsurface measurements to generate first estimates of the full subsurface profiles; and (*iii*) the dynamical model itself to adjust and interact the features and to interpolate between the features. The feature model for the Gulf Stream is based on analytic studies by Niiler and Robinson (1967) and the ring models taken from data analysis of Olson (1980) and Joyce (1984). A schematic sketch

of the three dimensional initialization, thin jet model, cold and warm ring feature models is shown in Fig. 1.

The Gulf Stream Feature-Model uses the same thin jet profile as RSP. The across-stream velocity component is identically equal to zero and the along-stream velocity component, μ, is written

$$\mu = \exp\left[-\frac{y^2}{g_0^2}\right] V_T \left\{\left(1 - \frac{V_M}{V_T}\right)\frac{z}{h_s} + 1\right\}, \quad z \geq -h_s$$

$$\mu = \exp\left[-\frac{y^2}{g_0^2}\right] V_M \left\{\left(1 - \frac{V_B}{V_M}\right)\frac{z - h_s}{H - h_s} + 1\right\}, \quad z < -h_s$$

where y is the across-stream coordinate, h_s (=1000 m) is the depth at which $\mu = V_M$ at the stream axis. V_T, V_M, V_B are the surface, base of the thermocline, and bottom values of the velocity along the stream axis which have been taken to be 165 cm s^{-1}, 25 cm s^{-1} and 5 cm s^{-1}, respectively. g_0 is the horizontal e-folding length chosen to be 40 km.

The Feature-Models for the cold and warm rings have been developed with free parameters to best fit the velocity structures of observed rings. The ring Feature-Models are characterized by four different parameters: $V_{\max}$, the maximum velocity in the ring; $r_{\max}$, the maximum radius of the ring; r_o, the radial distance at which the maximum velocity is reached; and $z_{\max}$, the maximum depth of the ring. In Fig. 1 the profiles used in this paper are schematically represented as a function of these parameters and of the radial distance. The horizontal structure is composed of a linear function up to $r = r_o$ and for $r > r_o$

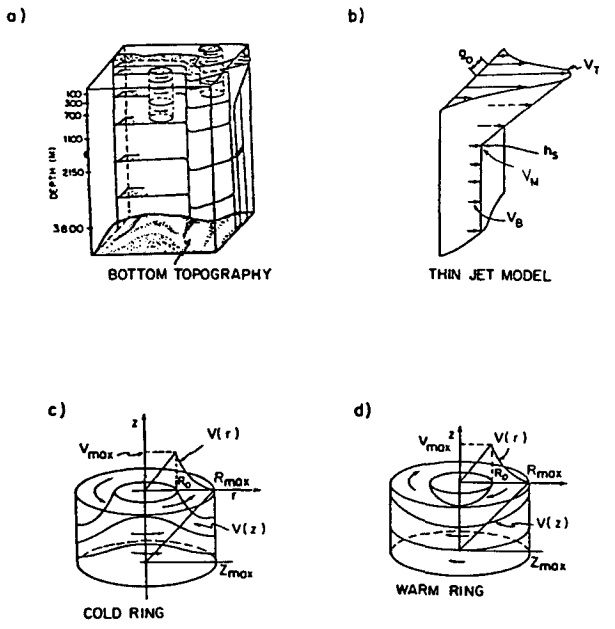

FIG. 1. Feature models: (a) three-dimensional schematic, (b) thin jet profile, (c) cold ring, (d) warm ring.

TABLE 1. Ring feature model parameters.

Ring	$V_{\max}$ (cm s^{-1})	R_0 (km)	$R_{\max}$ (km)	$z_{\max}$ (m)
$C1$	175	60	100	1000
$W1$	157	60	100	1000
$W2$, $W3$, $W4$	133	45	70	800

$$v(r) = V_{\max} e^{3(1-r/r_o)}.$$

The maximum velocity at each depth is linearly interpolated from $V_{\max}$ at the surface to zero at $z = z_{\max}$. The values for the parameters used in the cold and warm ring models are given in Table 1.

There are three major dynamical processes as the model integrates forward in time: adjustment, interpolation, and evolution. The first and second are associated with the feature-model initialization procedure and involve the adjustment of the feature structures and the filling in of the initially motionless fields between them, which involve vorticity interaction as the initial features feel each other's presence. During the third phase, the adjusted and interpolated fields evolve under mature ring–stream and ring–ring interactions and meandering events as determined by the physics of the governing equations subject to the initial and boundary conditions. This phase takes place over time scales of days to weeks and may result in the formation of new features or the destruction of features present in the initial condition.

4. SST data: 23 November–19 December 1984

The dataset on which these hindcast studies are based consists of the NOAA SST maps for the period of 23 November to 19 December 1984 (McHugh and Clark 1984). A detailed description of the SST analysis is given by RSP; only a brief summary will be included here. On 23 November, Fig. 2a, the Gulf Stream contains several small crests and troughs and one large crest near 57°W. The crests are labeled as N_1, N_2, etc. and the troughs are labeled as S_1, S_2, etc. from west to east. There are four warm rings to the north (W_1, W_2, W_3, and W_4) and one cold ring to the south (C_1). As the stream evolves the meanders grow and propagate to the east. There are several warm ring–stream interactions to the north and ring C_1 has been eliminated from the NOAA IR charts because it had not been observed for one month. A new warm ring is formed at 57°W between days 19 and 24. A new cold ring is formed at 62°W between days 17 and 26. On 19 December the Gulf Stream is relatively flat with a small crest at 60°W. More accurate times of ring formation are not available due to cloud cover.

5. PE and QG simulations

In this section, the PE and QG models are applied to the dataset described in section 4. The feature models

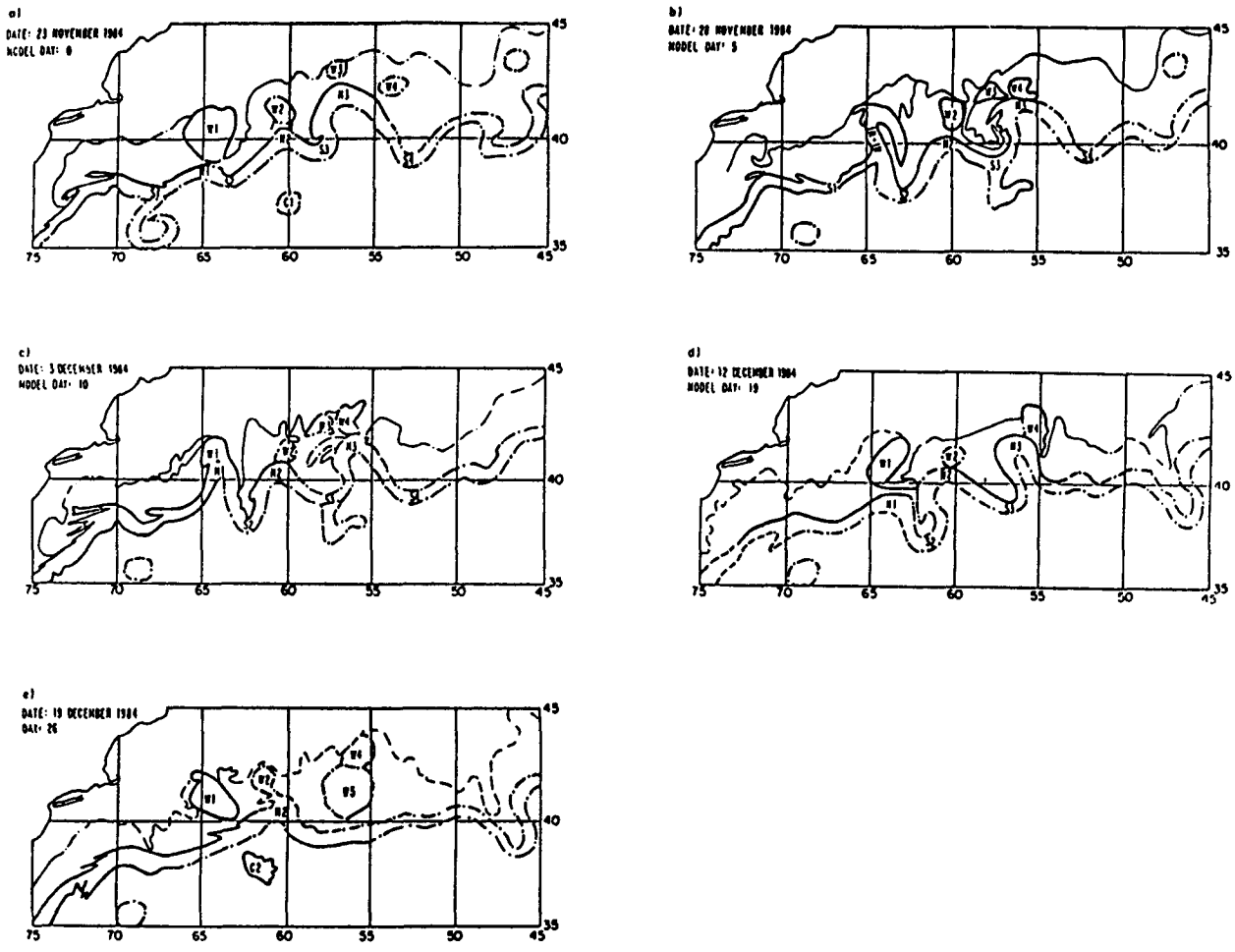

FIG. 2. NOAA SST analysis charts with surface fronts marked, see text. (a) 22 November 1984, (b) 28 November 1984, (c) 3 December 1984, (d) 12 December 1984, (e) 19 December 1984; forecast days are also indicated.

described in section 3 are used to initialize the models. The inflow and outflow boundary conditions have been persistent for the duration of the experiment, with the exception of the advection of vorticity on outflow as described in section 2. The model calculations will be referred to as QGF, PEF, QGT, PET for the quasi-geostrophic flat bottom, primitive equation flat bottom, quasi-geostrophic with topography, and primitive equation with topography, respectively. Because the large-scale frontal information is essentially the same at 100 and 300 meters, the model temperature field at 300 m will be used to indicate the location of the model Gulf Stream for discussion and comparison with the observed sea surface temperature.

We have chosen to retain the boundary conditions in these calculations although the time for a parcel of water in the core of the Gulf Stream to transit the model domain is less than the duration of the experiments, approximately 10 days. The model domain has been chosen such that the inflow location and direction of the stream is relatively constant over the one-month period under study so that continuing the inflow conditions is not a bad approximation to the large scale evolution. There of course could be small scale variability present which is not resolved by the satellite IR data and not included in our persisted boundary conditions. The outflow position of the stream is not well known due to cloud cover and, as such, information for updating the outflow boundary conditions was not available. These are inherent shortcomings of using sea surface temperature as a single source of data for boundary conditions.

The influence of bottom topography will be studied by comparing the flat bottom calculations in section 5a with those which include bottom topography in section 5b. As can be seen in Fig. 3, the New England Seamount Chain runs through the model domain. The seamounts are very tall, O(3000 meter), and steep, O(10%) grade, and have spatial scales of approximately 50 km. In section 5c, the calculations are discussed and comparisons are made with data, where applicable. The analysis includes both a qualitative description of

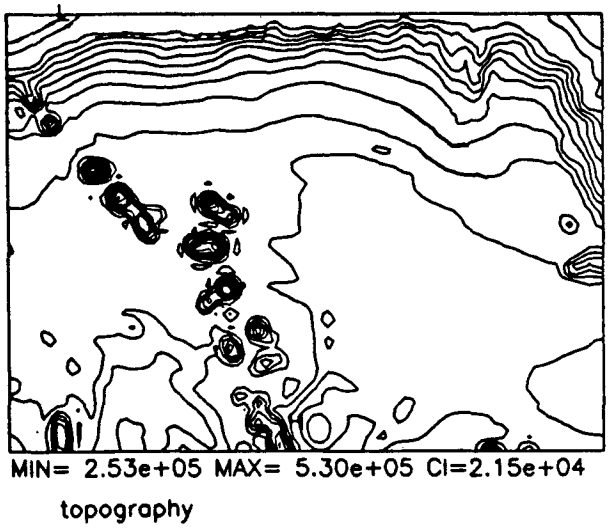

FIG. 3. Bottom topography.

the upper-thermocline temperature fields and deep velocity fields and a more quantitative study of the kinetic energy spectra.

The initialization technique used to obtain temperature and salinity from density anomaly (or quasi-geostrophic streamfunction) takes into account variable T–S relationships within the domain. In a region such as the Gulf Stream, the T–S characteristics vary considerably from the Sargasso Sea to the slope waters, Fig. 4. In the model initialization, each parcel of water in the domain is determined to be some portion of Sargasso Sea water and some portion of slope water. The T–S relationship for that water parcel is then obtained by interpolating along a surface of constant density between the slope and Sargasso T–S curves. The temperature and salinity are derived such that the appropriate T–S relationship is obeyed and the desired density is obtained when used together with the equation of state. Details of the technique are given in SR.

The PE model was initialized with the hybrid coordinate interface at 1600 meters, placing seven levels above the interface and three below. The QG model was initialized with the same nominal levels and average bottom depth.

a. Flat bottom: PEF, QGF

The temperature at 300 meters for run QGF is shown in Fig. 5 for selected days of the 30-day calculation. The initial evolution of the stream is slow; slight adjustments of the stream are visible near the edges of the jet and in the crests and troughs. On day 4, the meander growth and development is just beginning to take place. Four days later, the stream has evolved considerably. The trough near 63°W (S_2) has deepened 50 km and the crest just downstream is growing larger and extending to the north. The trough originally at 58°W has deepened 60 km and propagated to the east about 100 km. The large, broad crest at 57°W has become narrower and more elongated. On day 12, S_2 has deepened another 70 km and N_2 continues to grow to the north. Ring C_1 is beginning to interact with S_2. In the east, N_3 is beginning to form closed temperature contours as the crest develops and the upstream trough propagates to the east. After 16 days a new cold ring is beginning to form from trough S_2 and a new warm ring has just pinched off from crest N_3. The crest at 61°W has grown over 200 km and is now oriented in a north–south direction. Just downstream of the inflow position a large scale meander is also developing to the north. These same tendencies continue over the next 8 days, the meanders at 63° and 59°W continue to grow and the eastern meander eventually absorbs the new warm ring. As a result of this meander system, the new cold ring also strongly interacts with the stream.

The temperature at 300 meters for run PEF is shown in Fig. 6 at 4-day intervals. The early adjustment of the feature models occurs over the first few days; small changes in the structure of the initial rings and Gulf Stream are visible on day 4. The meander crests and troughs are also beginning to deepen and develop. There is a large patch of water being ejected to the west from the crest at 58°W. On day 8, the troughs at 62° and 57°W have deepened by approximately 50 km. Water from the edge of the Gulf Stream is being pulled from the base of the troughs and advected toward the west. The crest at 58°W has extended to the north by 40 km. Regions of strengthened temperature gradients are clearly visible along the stream. Over the next 8 days, the trough at 62°W continues to deepen and begins to close off temperature contours. The original cold ring C_1 is strongly interacting with the Gulf Stream. A small cold ring is formed from trough S_3 on

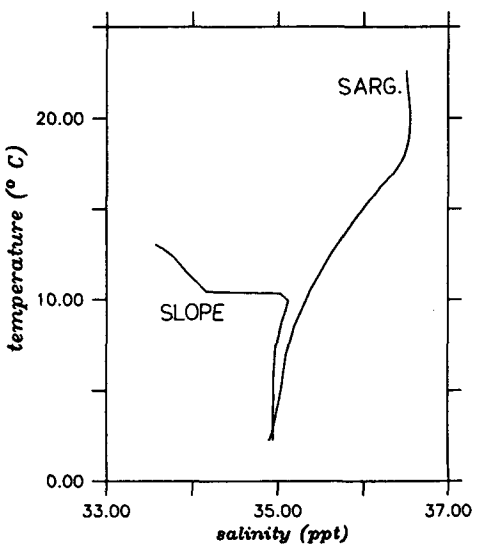

FIG. 4. T–S relationship in slope and Sargasso Sea waters.

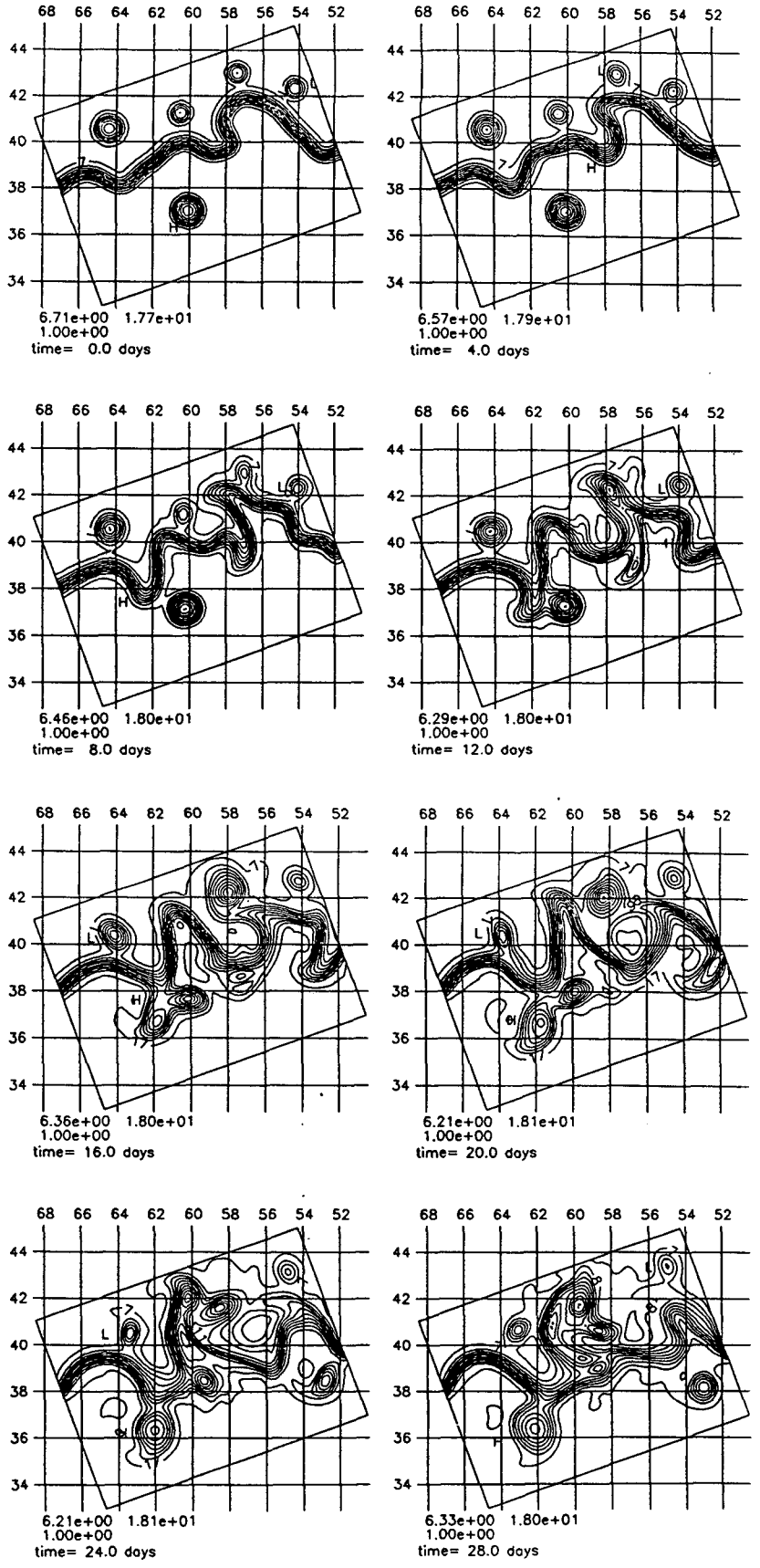

FIG. 5. QGF: Flat bottom, temperature at 300 meters.

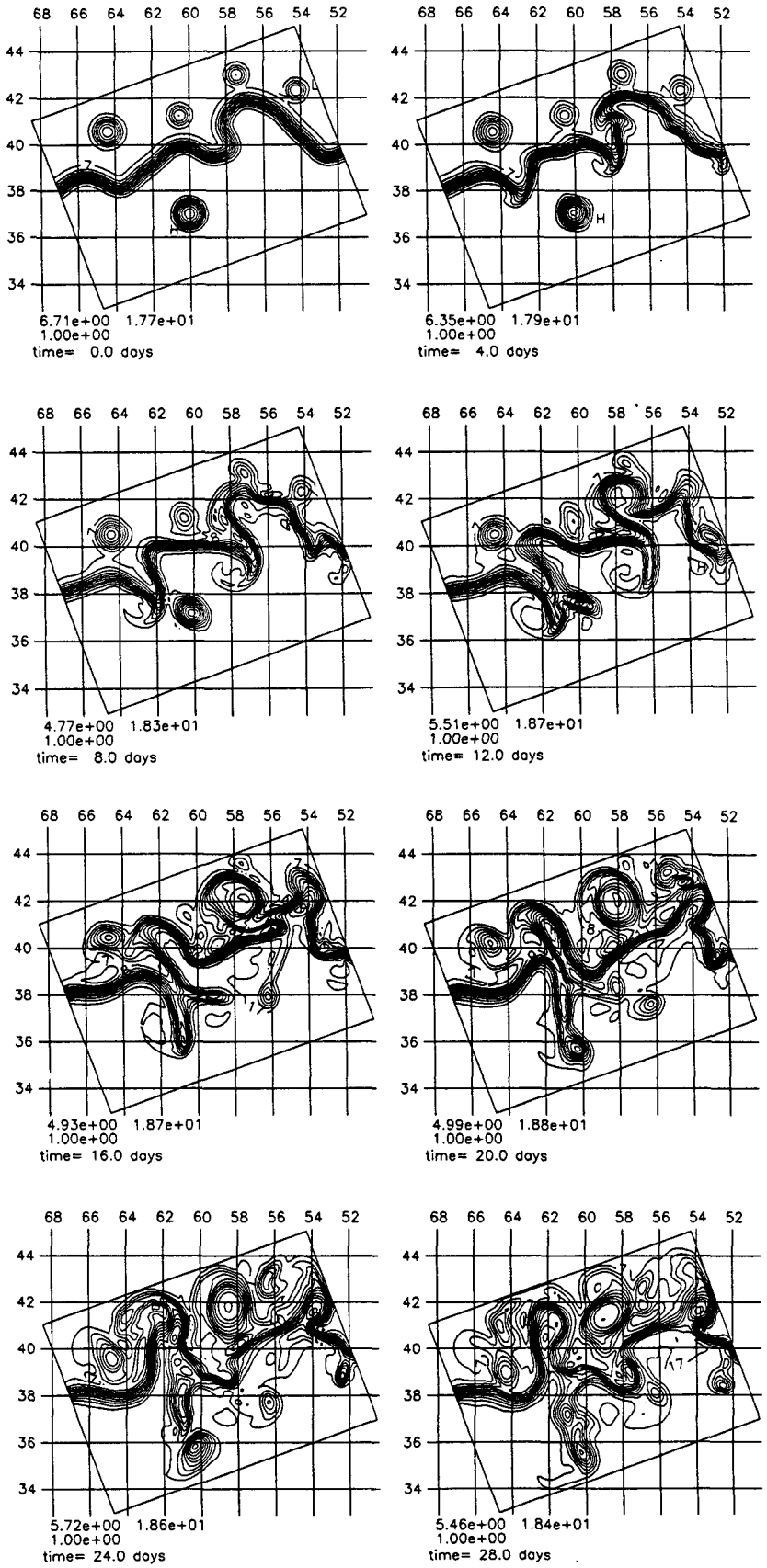

FIG. 6. PEF: Flat bottom, temperature at 300 meters.

day 16. The crest at 57°W is starting to form a warm ring as the upstream trough propagates to the west. Additional small scale variability is becoming visible adjacent to the stream. On day 20, the new warm ring W_5 has formed at 42°N, 58°W. Trough S_2 is now very deep and has closed several temperature contours. Over the next 8 days, the new cold ring forms but is quickly reabsorbed by the stream. The crest at 61°W extends all the way up over the continental slope and sheds a small warm ring. A new trough is beginning to develop at 58°W and interect with the small cold ring.

The velocity fields at 3850 meters on day 24 are shown in Figs. 7a and 7b for QGF and PEF, respectively. Day 24 was chosen because it is representative of the deep velocity patterns over the last two weeks of the integrations. The deep QG field is dominated by cyclonic and anticylonic large-scale circulations with weaker eddies of slightly smaller scales present. The maximum velocities are large, on the order of 30 cm s^{-1}. There is only weak evidence of the newly formed warm and cold rings and there is no strong Gulf Stream signature. Very little small scale activity is present throughout the model domain. The deep primitive equation velocities are much different, Fig. 7b. There is a great deal of variability on small scales, 50 to 200 km. These small eddies are quite energetic, with maximum velocities of 30 to 50 cm s^{-1}. There is also a larger scale circulation pattern, some of which is correlated with the surface signature of the Gulf Stream. There is a significant return flow along the northern part of the domain where the continental slope should be. In two locations near the outflow boundary there are strong velocities, which may be related to the outflow boundary condition. The new cold ring has a strong signature at this depth but the new warm ring does not. An analysis of the kinetic energy spectrum of these fields is discussed in section 5c.

b. *Bottom topography: PET, QGT*

In this section the PE and QG models were initialized with the bottom topography shown in Fig. 3. The temperature field at 300 meters for run QGT is shown in Fig. 8. The results are almost exactly the same as in the flat bottom calculation until day 16. The portion of the stream just past the inflow remains flatter and the developing crest at 61°W (N_2) is a little narrower in QGT than in QGF. During the next week the crest, which developed in the flat bottom calculation just past inflow, does not develop here; the stream remains very flat and smooth. The cold and warm ring formation events are not affected by topography but the new cold ring does not interact with the stream after formation. N_2 does not grow as large as previously and begins to be advected to the east. On the final day of the simulation the stream remains flat over most of the domain. A small warm ring was formed off of the crest at 61°W and C_1 and W_5 remain free from the stream.

The temperature for run PET at 300 meters is shown in Fig. 9 at four-day intervals. The first 16 days are essentially the same as in the flat bottom case. All of the major developments are reproduced with bottom topography. On day 20, some differences are visible in the region of the forming cold ring C_2. The addition of topography has facilitated the cold ring formation so that it separates from the stream more cleanly and, on day 24, the new cold ring is free from the stream. The continental slope appears to inhibit the northward growth of the crest at 61°W so that on day 28 it does not extend past 41°N. The addition of topography has affected the upper-thermocline temperature fields slightly, but the major dynamical events remain unchanged.

The deep velocity fields on day 24 for the QG and PE calculations with bottom topography are shown in Figs. 10a and 10b, respectively. The addition of bottom topography has changed the deep velocity fields in the QG model considerably. The two large scale circulations, which dominated the flat bottom calculation, are not generated here. There is a stronger zonal flow, which correlates with the position of the Gulf Stream in the upper ocean, and there is considerable return flow along the edge of the continental shelf. There is also evidence that the topography is acting to direct the flow around the New England Seamounts. Locations at which the actual depth is less than 3850 m are enscribed. Velocities directly over the tall topography are only a few centimeters per second or less. The addition of topography has also changed the deep PE fields, Fig. 10b. The larger scale circulations present in the flat bottom case are greatly reduced here. The flow pattern is populated with very small scale eddies and jets. There is still some signature of the Gulf Stream and cold ring, but it is weaker and not as consistent. It is clear that the seamounts are acting to direct the deep flow, resulting in strong local jets adjacent to the topography. There is some return flow along the continental slope but it does not extend up over the strong topography as it did with a flat bottom. Again, velocities are quite strong with local maximums between 30 and 50 cm s^{-1}. This strong mixing may be responsible for the homogenization of deep water properties as hypothesized from hydrographic data by Bower et al. (1985). An analysis of the kinetic energy spectra of these fields is discussed in section 5c.

c. *Discussion*

The PE and QG models behaved very similarly over the first two weeks of integration in terms of the feature model adjustment and large-scale meander evolution. Between two and three weeks of integration, the meander patterns in the models are similar but differences are seen in the ring formation events. After three weeks, the meander system in the PE model begins to diverge from both the QG model and the observed sea surface

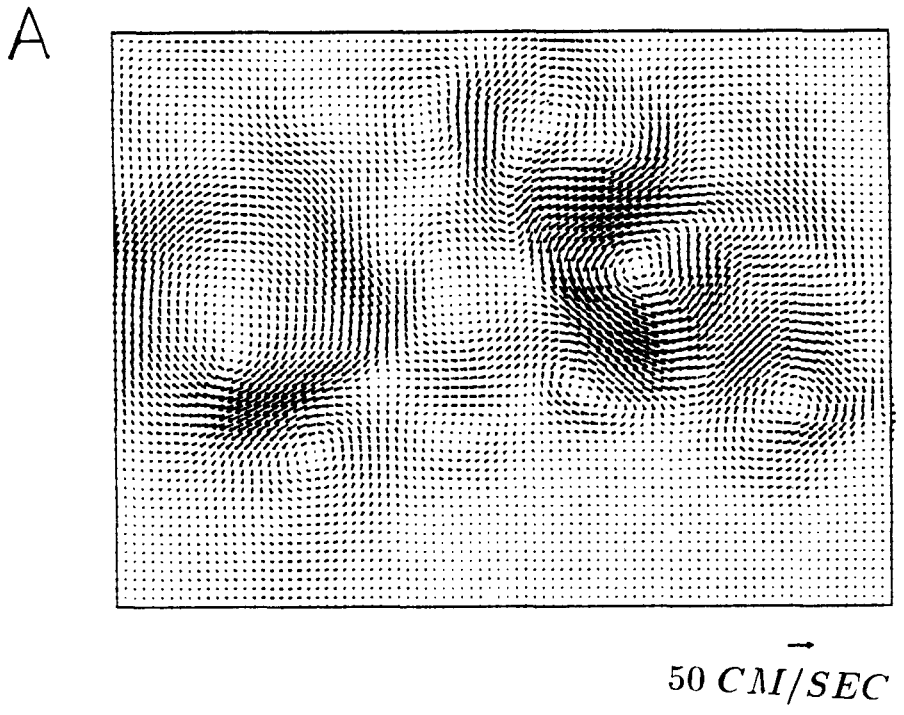

FIG. 7. Velocity at 3850 meters (a) QGF; (b) PEF.

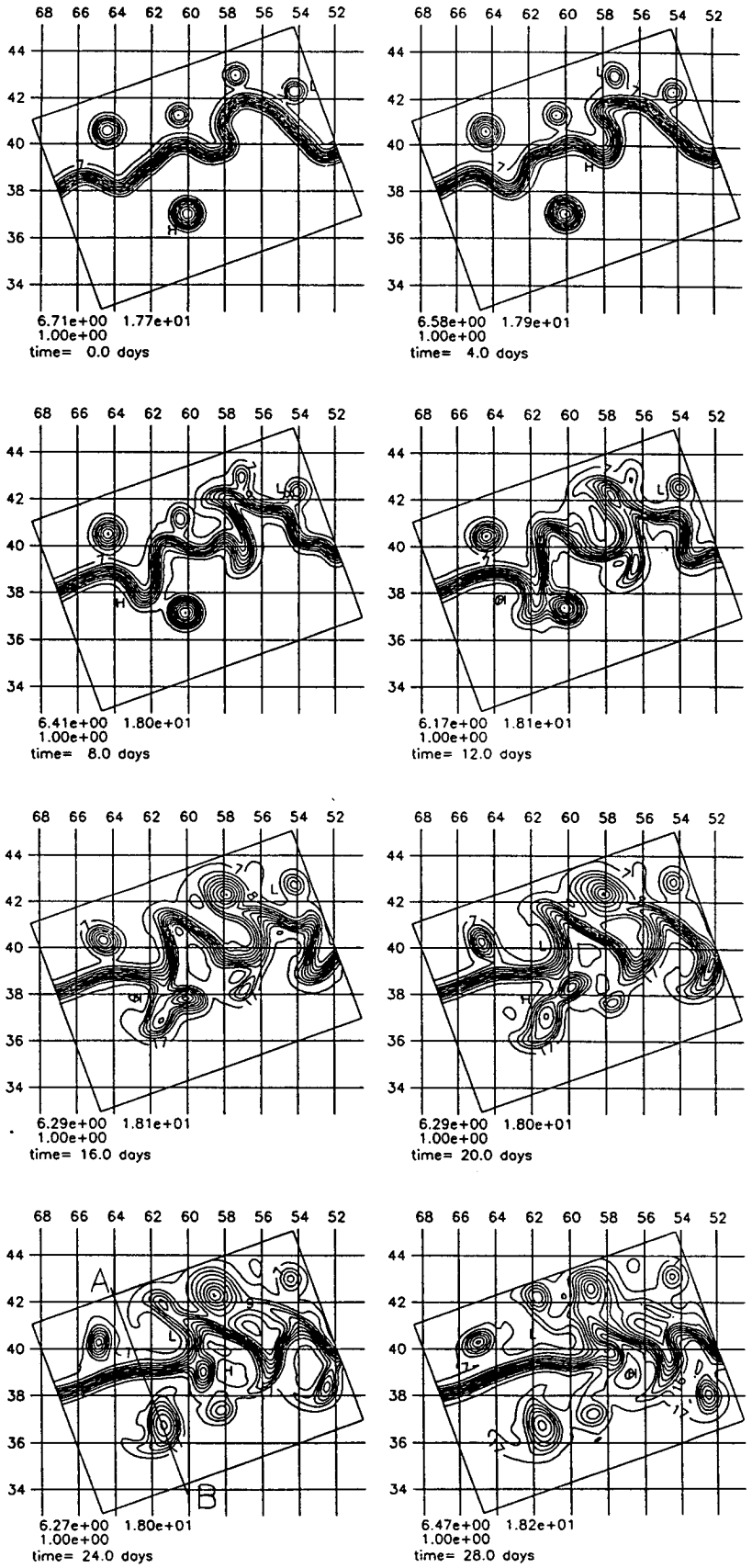

FIG. 8. QGT: Bottom topography, temperature at 300 meters.

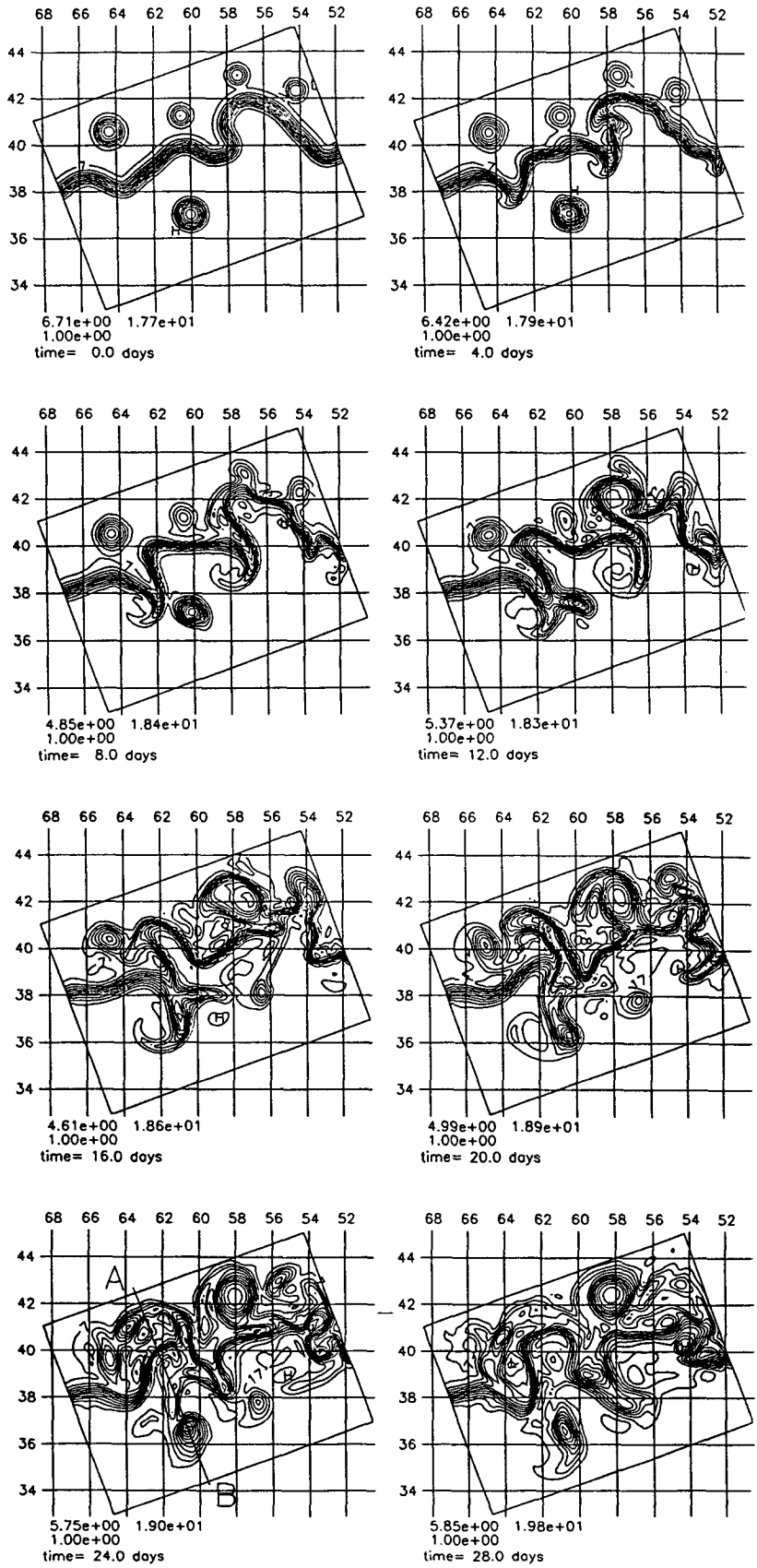

FIG. 9. PET: Bottom topography, temperature at 300 meters.

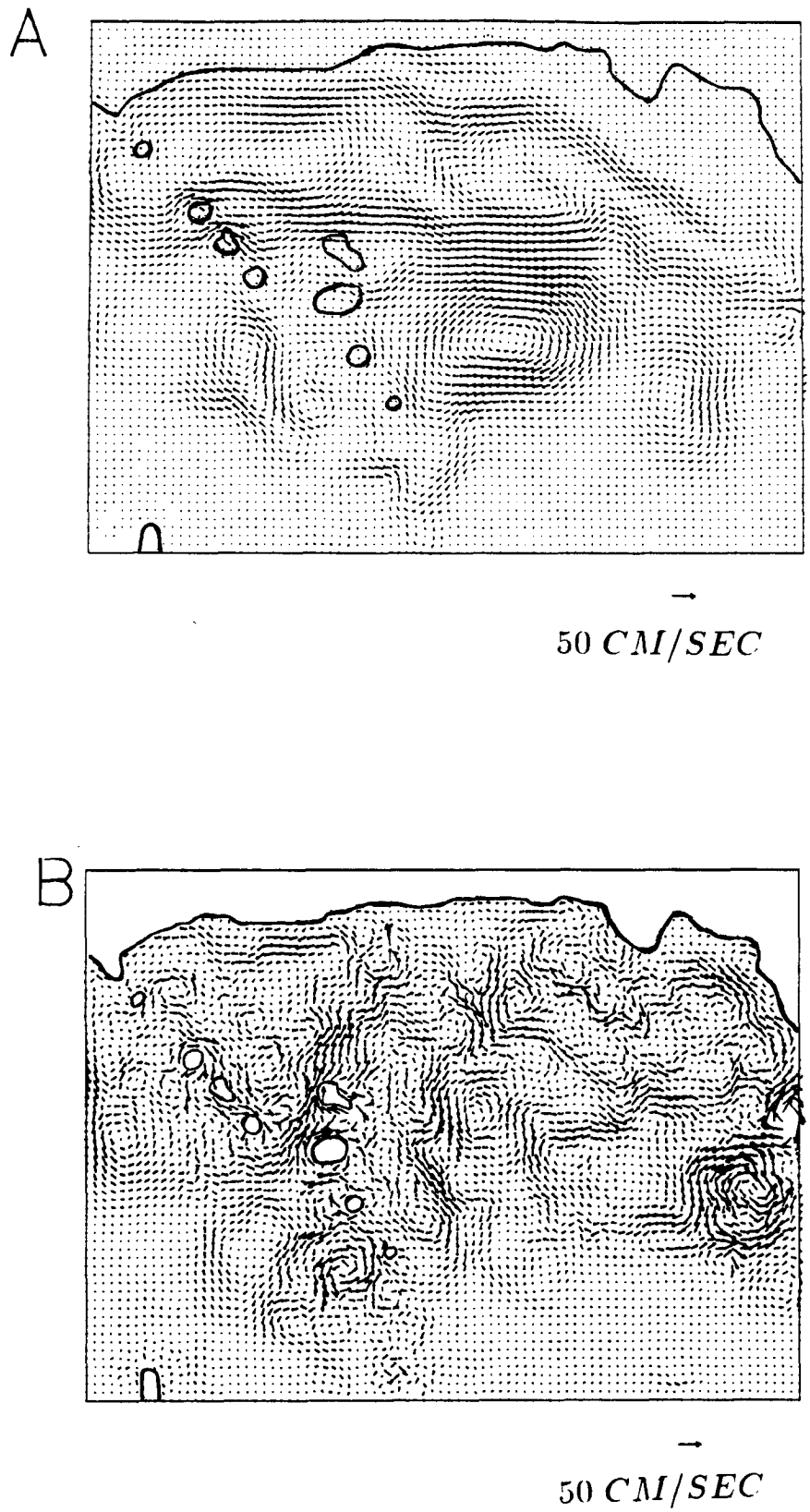

FIG. 10. Velocity at 3850 meters (a) QGT; (b) PET.

temperature. There are, however, some interesting differences in the early adjustment period, warm and cold ring formation events, deep velocity fields, and general behavior and characteristics of the simulations which deserve further discussion. An analysis of the kinetic energy spectra in the midthermocline and deep ocean will be used to study the dependence of the flow scale to the model physics and presence of bottom topography. A discussion on the role of bottom topography and the validity of the quasi-geostrophic approximation in the region is also presented. Finally, several interesting features generated by the numerical models are compared with each other and data, where applicable.

1) KINETIC ENERGY SPECTRA

The two-dimensional kinetic energy spectra was calculated at 300 and 3850 m for the four model calculations discussed in the previous section. In order to obtain periodic boundary conditions in the zonal direction without modifying the meridional structure of the Gulf Stream, a mirror image of the stream was projected across the eastern boundary, thus generating a model domain that was $2(M-1)$dx (2700 km) long. To avoid a discontinuity at the boundaries, the model domain was extended by several grid points and the meridional velocity interpolated to zero at the extended model boundaries before producing the mirror image. Because the inflow/outflow boundary conditions were chosen to be nearly zonal and the same method was used in the analysis of each model field, it is not believed that any significant aliasing of the kinetic energy fields has resulted from this technique.

The kinetic energy density as a function of wavenumber is shown in Figs. 11a and 11b on day 24 for depths 300 and 3850 m, respectively. The overall energy distribution at 300 m is very similar for each of the runs with a peak between wavenumbers 6 and 10 and a k^{-3} decay at large wavenumbers. However, a closer look reveals some differences due to both model physics and the presence of topography. The largest scales are similar but PET has considerably less energy at wavenumbers 3–4 (wavelengths 900–1350 km) than the other runs. The intermediate scales (wavenumbers 5–8) are similar for both PE calculations, but the QG calculations are quite different. QGF has a strong peak of 2000 $cm^2 s^{-2}$ at wavenumber 7 (450 km) compared to 600 $cm^2 s^{-2}$ for QGT. This peak corresponds to the large meander system which was discussed in the previous section. All of the models behave similarly between wavenumbers 8 and 30 (385 to 93 km), although both PE fields are stronger than the QG fields at the lower wavenumbers. These wavelengths correspond with the width of the Gulf Stream, near field circulations, and Gulf Stream rings and reflect the fact that the primitive equation fields contain stronger frontal regions. There is a very clear separation between the PE fields and the QG fields at small wavelengths, above wavenumber 30. Both PE calculations contain much more energy at the small scales than do the QG fields. Topography has very little affect on this separation. The only significant effect of topography on the upper-ocean kinetic energy spectra was to eliminate the peak at wavenumber 7 in the flat bottom QG calculation.

A linear quasi-geostrophic stability analysis was done on the basic feature model profile with a flat bottom using the analysis procedure of Beckmann (1989). The fastest growing unstable mode has a zonal wavelength of 410 km. The stability curve is very flat between 333 and 500 km such that growth rate at 450 km is only 1% less than the fastest growing mode. It is possible that the 450 km wave became dominant because the 1290 km domain allows a resonance of wavenumber 3 with the inflow/outflow boundary conditions acting as nodal points. The addition of topography changes the stability characteristics of the jet and may have resulted in the breakdown of the peak in kinetic energy. It is also possible that varying the inflow/outflow boundary conditions with time may inhibit the growth of this wave. These comments are only speculative and more study is needed on the relationship between meander growth and initial conditions, boundary conditions, and the presence of topography.

The deep kinetic energy spectra are shown in Fig. 11b. QGF and PET (curves A and D) have very little energy in the uniform flow but, as was reflected in the velocity maps, this is for very different reasons. QGF was dominated by two large scale circulations and PET was dominated by highly variable, small scale eddies and jets. The representation of the Gulf Stream in the deep in both the PEF and QGT (curves B and C) is reflected by their higher energy levels for the uniform flow. Between wavenumbers 2 and 7 (2700 to 450 km) the flat bottom calculations contain consistently higher kinetic energy than the calculations with bottom topography. This is due to the basin-scale circulations seen in both flat bottom calculations. The bottom topography acts to break up these large coherent patterns. Since it is seen with quasi-geostrophic physics, this break up is at least partially due to the stretching term. It is not clear if the significantly lower kinetic energy in the primitive equation fields is due to extra physics in the primitive equations or the more accurate treatment of the bottom topography. At wavenumbers greater than 15 (200 km) there is again a clear separation between the model results. As was seen in Fig. 7, QGF contains very little small scale energy. The addition of bottom topography to the QG model increases the energy at wavelengths between 200 and 50 km but does not have any significant affect for wavelengths less than 50 km (wavenumber 55). This is approximately the horizontal scale of the New England Seamounts and other small scale variations in bottom topography. Flow at scales much less than 50 km would violate the QG approximation. The addition of topography is seen to affect the PE fields in a similar way.

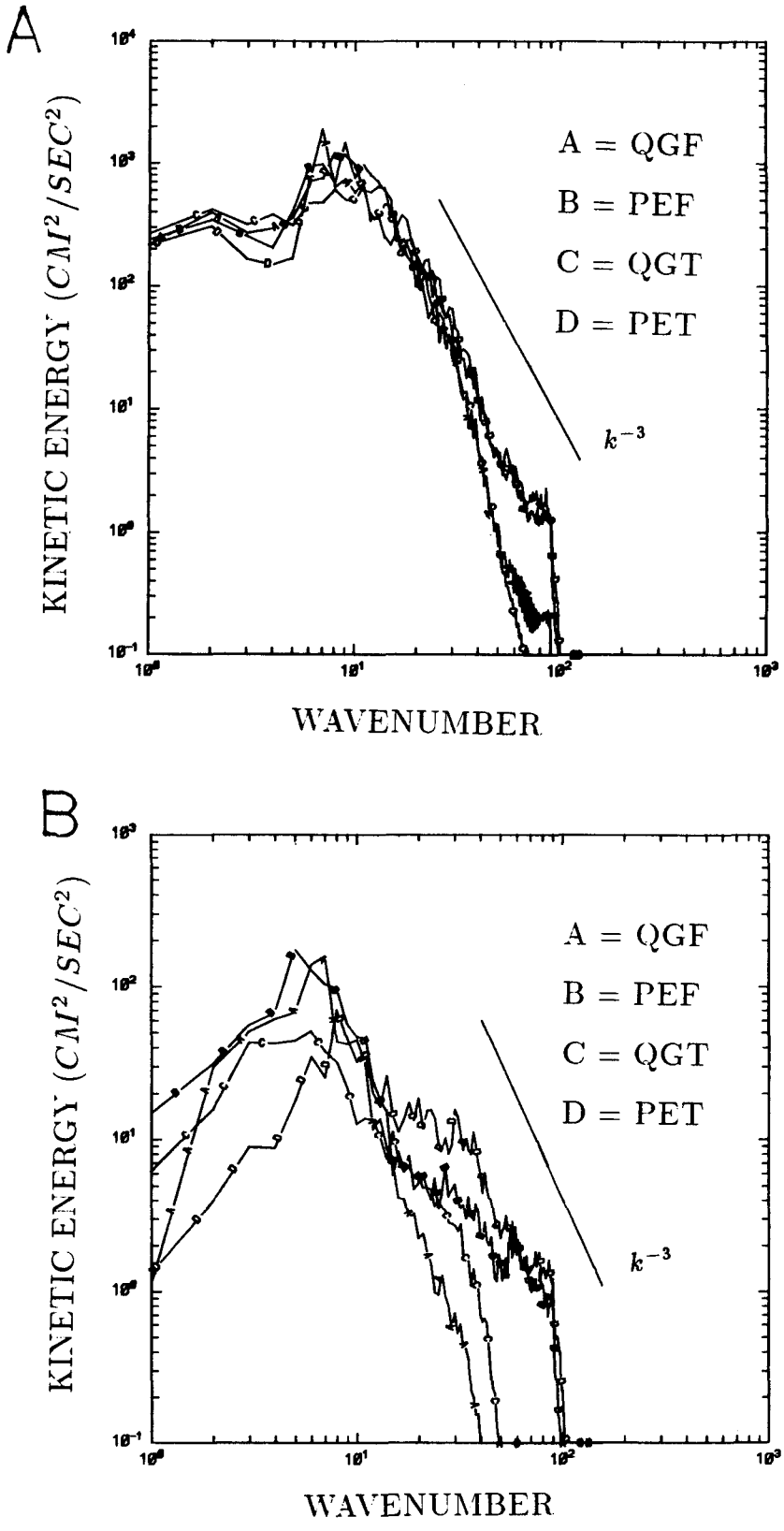

FIG. 11. Kinetic energy spectra (a) at 300 meters; (b) at 3850 meters.

Run PET contains significantly more kinetic energy than PEF and both QG calculations between wavelengths 200 and 50 km. At very small wavelengths (less than 50 km) both PE calculations have energy which is not contained in the QG fields.

There are two processes competing at the small scales in the deep ocean. Primitive equation physics contain more instability mechanisms and admit higher Rossby number (smaller scale) flow than does quasi-geostrophy and as a result generates more small scale variability, both with and without topography, than does quasi-geostrophy. This effect is dominant at wavenumbers greater than 15. The addition of bottom topography increases the kinetic energy between 200 and 50 km in both models but has almost no effect at smaller scales. This band of 200 to 50 km corresponds to the horizontal variations of the bottom topography shown in Fig. 3. This cascade to smaller scales is consistent with the topographic scattering discussed by Rhines (1977) and Haidvogel (1983).

2) Implementation of bottom topography in the QG model

Bottom topography can influence the flow field in several ways. Conservation of potential vorticity, which is included in quasi-geostrophic physics, will cause the flow to follow lines of constant $(f + \zeta)/H$. This is consistent with the inhibition of the meander growth to the north over the continental slope topography seen when bottom topography was added to both the PE and QG models. The steering of the deep flow fields around the New England Seamounts is also partially accomplished by this stretching term because it was seen to some extent in the deep QG fields.

In addition to providing vortex stretching, the primitive equation bottom topography can act as a physical blocking mechanism for the flow. When flow encounters topography, the parcels may go over or around the feature. In order for the flow to go over, the kinetic energy of the water parcel must be large enough to lift the parcel through the water column against the force of gravity. This height may be approximated as $\Delta = u/N$ (Gill 1982); bottom topography that is taller than Δ will effectively block passage of the water parcel. In this case, for narrow topographic features such as the New England Seamounts, the flow will generally go around the topography. Flow will tend to go over the feature in regions of large horizontal velocity and weak stratification. For the Gulf Stream region $\Delta = O(10^3\ \text{m})$.

The quasi-geostrophic equations contain an order Rossby number approximation to the full energy constraint on the movement of a water parcel. However, because the lower boundary condition is applied at the mean bottom depth, the kinematic constraint of no flow through the physical bottom is not present in the quasi-geostrophic model. If the energy is not sufficient to lift the parcel over the full height of the topography, the parcel may either go through or around the topography. The extent to which the parcel goes around the topographic feature is dependent on the size of the vortex stretching term (which is contained in quasi-geostrophy) compared to the vertical advection terms (which are neglected). For flow which goes over the location of tall topography, the bottom boundary condition may result in vertical velocities at the mean bottom depth that exceed the QG scaling assumptions. If the flow is steered around the topography by the stretching term alone, causing the vertical velocity to be small, the QG approximation remains valid.

The vertical velocities imposed as the lower boundary condition in the QG run with topography were calculated from Eq. (14) over the final 14 days of the simulation. The maximum allowable vertical velocity from equation 15 is 0.036 cm s^{-1}, with $V_0 = 30$ cm s^{-1}, $H_0 = 1000$ m, $f_0 = 1.0 \times 10^{-4}\ s^{-1}$, $d = 50$ km. The average magnitude of the vertical velocity imposed at the bottom of calculation QGT is approximately 0.01 cm s^{-1}. Approximately 5% of the bottom points have vertical velocities greater than those allowed by the QG approximation. Of those points, the average magnitude of the vertical velocity is approximately 0.1 cm s^{-1}, with values as large as 1 cm s^{-1}. This is significantly larger than the QG approximation allows and indicates that possibly important vertical advections are being neglected.

In spite of these inadequacies, quasi-geostrophic physics did modify the deep fields and, to some extent, steer the flow around tall topography. In addition, the bottom topography broke down the large, basin-scale deep circulation and added kinetic energy in the smaller scales, similar to the behavior of the primitive equation model. Although the QG approximation may neglect terms in the presence of steep and tall topography, based on this study it is better to treat the topography in its true form rather than to truncate or filter it. The vertical advection of the mean density profile is included in the QG equations and may play an important role in determining whether the flow is to go around or over the topography.

3) Model and data comparisons

In this section, several features generated by the numerical models are described and compared with historical data. The discussion is separated into the following sections: warm water outbreaks; meander growth rates; velocity structure at the base of the thermocline; and warm and cold ring formations.

(i) *Warm water outbreaks*

Long trailing filaments of Gulf Stream water are seen extending from the meander troughs in the PE temperature fields beginning on day 8. These features are

largest near the surface (100 m) but also have signatures further down in the water column (700 m). Similar temperature signatures are commonly observed in satellite IR imagery. Cornillon et al. (1986) has studied images for a three year period and classified four types of these warm water outbreaks. The size of the outbreak predicted in the model calculations agrees well with those observed by Cornillon, roughly 100 km × 200 km. The structure of the temperature signal seen here is most like the class A outbreak defined by Cornillon although each of the other three classes identified also originate at the base of the meander troughs but are modified by nearby cold rings or extreme Gulf Stream meanders.

Through analysis of the SST alone it is not clear whether these filaments are being advected from within the Gulf Stream core or being pulled from the stream by adjacent circulations. Figure 12 shows a superposition of the temperature and the velocity at every other point at 100 m in the vicinity of the deepening meander S_2. The core of the Gulf Stream jet and presence of the near field circulation are clear in the velocity field. Because the near field circulations are barotropic, there is no direct signature in the temperature field, only the signature of the SST as a passive tracer. Based on this analysis, it appears that the warm outbreak is generated by the anticyclonic circulation pulling water from the southern edge of the stream into the Sargasso. Anticyclonic circulation has been measured in warm outbreaks by a Climate Air–Sea Interaction Drifter (CASID) satellite tracked drifting buoy (Large et al. 1986). Magnitudes at 120 m ranged from about 15 to 50 cm s^{-1} and showed a strong correlation with the sea surface temperature. This is in good agreement with the velocities produced by the PE model.

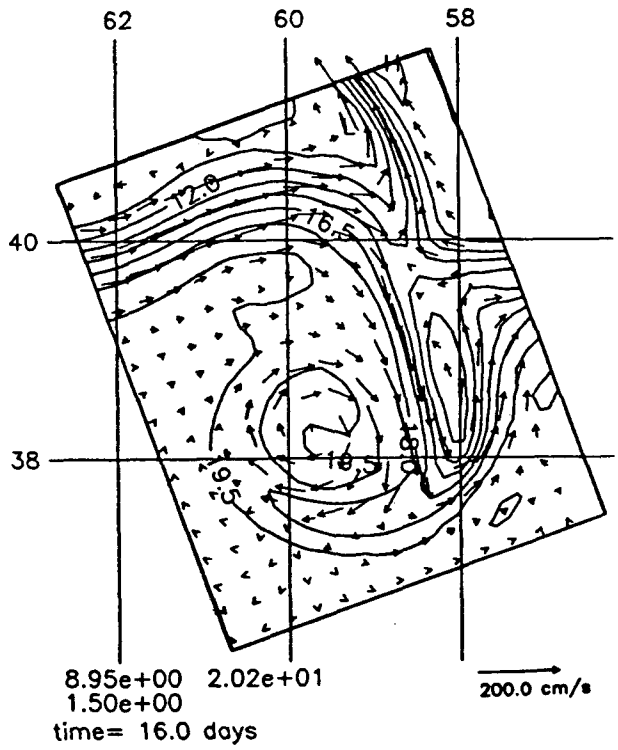

FIG. 12. PET: Temperature and velocity of meander and near-field circulation.

(ii) *Meander growth rates*

Much later in the calculations, after day 20, some interesting and significant differences arise between the PE and QG model calculations and the observations. Up to day 20, the model simulations are similar in structure and location of the stream; the differences are mostly related to time of ring formation and phase of the Gulf Stream meanders. By day 24, however, a large meander is developing in the western portion of the PE calculation which is not seen in either the QG calculation or the observations. Over the next four days the meander continues to grow and takes on a somewhat uncharacteristic squared shape. The growth of this meander is accompanied by a tightening of the temperature contours, indicative of strong frontogenisis events, which are possible with PE physics. The stream in the QG calculation remains smooth and flat out to 60°W, comparing well with the observed stream location. It is interesting that the location of this large meander is just upstream of the New England Seamount chain. Its development may be coupled to the large meandering and ring formation event that occurred over the seamounts just prior to day 24. The growth of this large meander may also be related to errors in the initial/boundary conditions. The similarity of the PE fields with the QG fields and the observed stream location over the first 24 days and the realistic ring formation events produced by the PE model suggest that the growth rates of any errors in the initial conditions are small. The affect of using a dynamically adjusted initial condition for the PE model is investigated in section 6.

In the eastern portion of the domain both the PE and QG fields develop a small-scale wave pattern along the stream. Although there is a slight indication of such waves in the observations, the waves in the model calculations appear to be related to the outflow boundary condition. However, over the four week duration of these calculations, the waves remain within 200 to 300 km of the eastern boundary. The influence of the outflow boundary condition on the interior solution needs to be studied as a function of initial condition and length of model integration.

(iii) *Velocity fields at 1100 meters*

The velocity fields at 1100 m on day 24 are shown in Figs. 13a and 13b for runs QGT and PET, respectively. At this level the fields are quite complex and

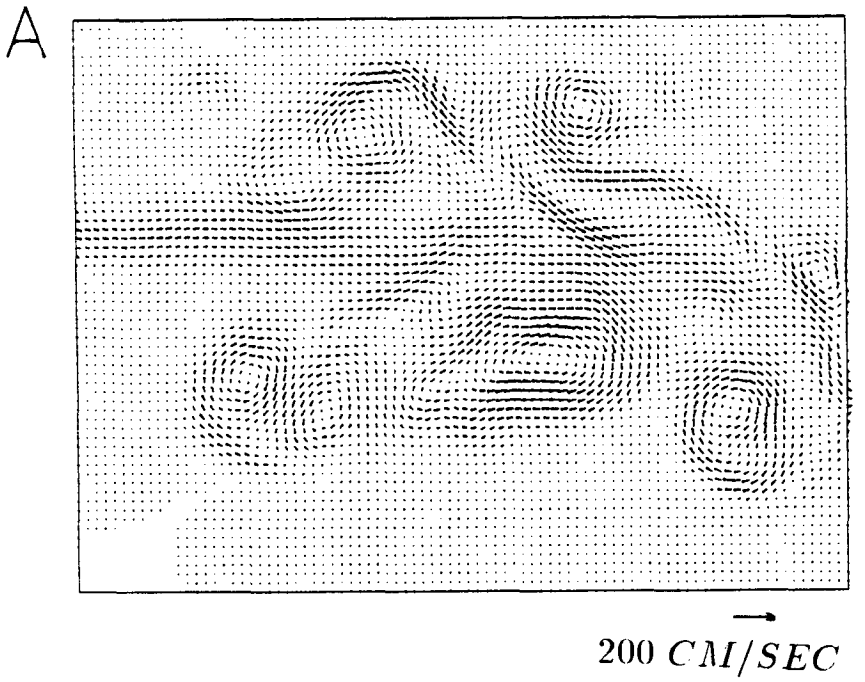

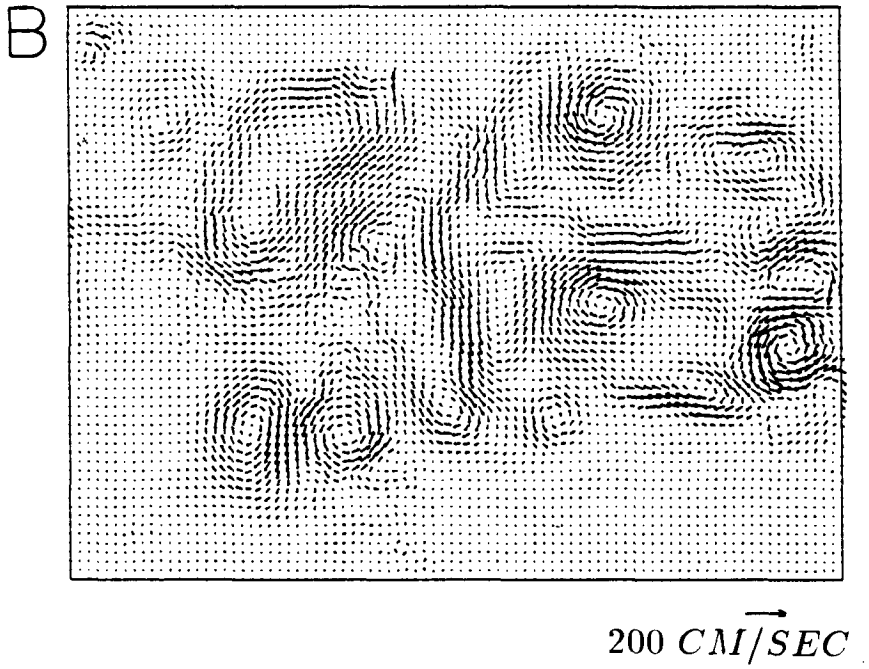

FIG. 13. Velocity at 1100 meters (a) QGT; (b) PET.

energetic. There is a strong signature of the Gulf Stream jet [O(40 cm s^{-1})] throughout the region in QGT. In addition, there are circulations adjacent to the stream and rings which were spun up during the course of the calculation. The cold ring near-field circulation is clearly visible in the southeast region of the domain. At this level, the near-field circulation is slightly stronger than the cold ring. The primitive equation velocity fields also have a strong signature of the Gulf Stream jet but contain more intermediate and small scale eddies. The maximum velocities are slightly stronger than in the QG field [O(40–50 cm s^{-1})]. The new warm and cold rings have stronger circulations in the PE fields than in the QG fields.

It is clear that the simple deep fields used to initialize the model calculations evolve in a very complicated way and generate many energetic eddies and jets. The pattern of a float put into the stream at this depth could be very complicated and convoluted. At times it might appear to follow the upper-ocean signature of the Gulf Stream but then get entrained into one of the adjacent circulations, which are strongly barotropic and have little surface temperature signature. Features of the type seen here may help to explain the highly variable and sometimes erratic behavior of floats in and near the Gulf Stream.

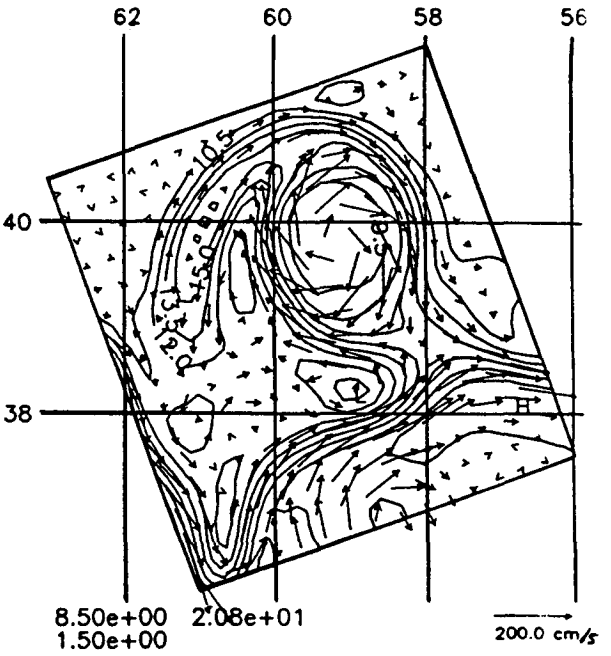

FIG. 14. PET warm ring: (a) velocity at 100 meters, day 16; (b) temperature and velocity at 100 meters, day 21.

(iv) *Warm ring formation*

Both the PE and QG models produce warm ring W_5 in good agreement with the observed data, but there are some interesting differences in the ring formation processes. On day 12, the meander that forms the warm ring is just beginning to close temperature contours in both calculations, Figs. 9, 8. In the PE fields the meander has taken on a round, looped shape by advecting the downstream portion of the meander back to the west. This acceleration of the neck formation is not seen in the QG simulation. Four days later both calculations have almost formed the warm ring, but the ring in the PE model is much larger and contains warmer water (17° compared to 15°C).

Soon after formation the PE ring rotates clockwise at about 7 deg/day. A large patch of warm water is shed off the northern edge of the ring and is advected counterclockwise toward the Gulf Stream. This clockwise rotation and trailing streamer are very characteristic of observed warm core rings. The warm water in the streamer is just being ejected from within the ring on day 16. A superposition of the temperature and velocity fields on day 21 (Fig. 14) shows the streamer and the underlying velocity field advecting the temperature to the south. The streamer has temperature and velocity signals down to 700 m. It is possible that the shedding of water from warm rings is an adjustment to rings that are too large and strong to remain stable. In warm core rings, cyclostrophic accelerations act together with the pressure gradient to balance the Coriolis force. The cyclostrophic term is proportional to the velocity squared. A ring which has large velocities, O(200 cm s^{-1}), may become unstable and cause a rupture of the flow normal to the circumference of the ring, such as seen here.

Temperature and velocity sections taken through the PE and QG rings on day 24 are shown in Fig. 15 together with sections taken by Joyce (1984) through ring 81D. Both model rings compare well, but the temperature in the center of the PE ring is in better agreement with ring 81D. The velocity of the PE ring is the right magnitude, but the QG ring is a little too weak. The model rings are about the right size in diameter, 250 km, and have strong signals down to 1000 m. The PE ring was somewhat larger when it was formed but it was reduced in size when it formed the streamer.

(v) *Cold ring formation*

The models also produce a new cold ring, which is in good agreement with the satellite IR, but again there are some differences in the model formations. The early development of the meander and near-field circulation is seen in both models. The orientation of the deepening PE meander is slanted toward the west, and as a result ring C_1 interacts strongly with the stream. The PE ring formation is slower than the QG ring, but the exact time of formation is difficult to determine. The newly formed PE ring is smaller in diameter, but it has a

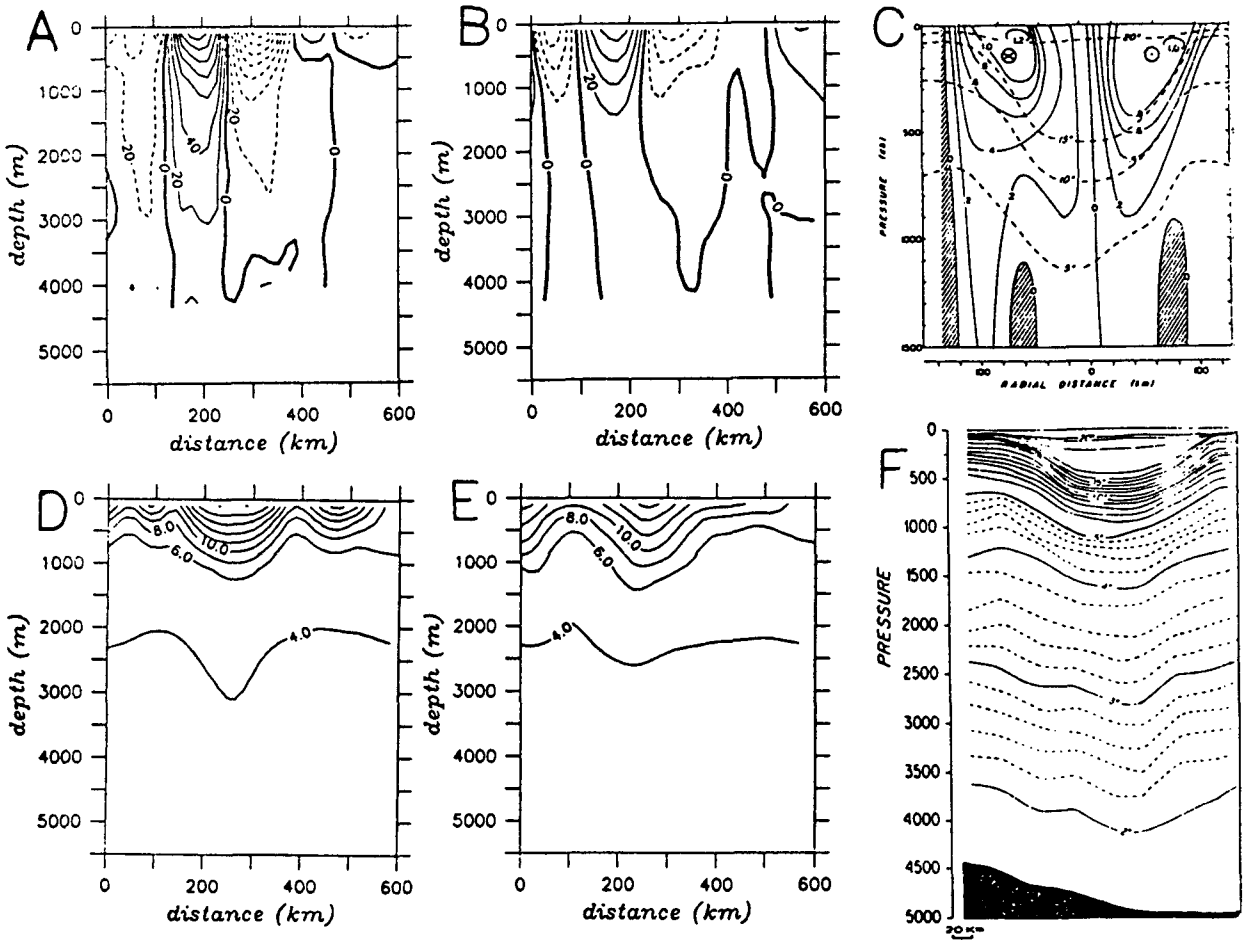

FIG. 15. Vertical sections: (a) velocity PET, (b) velocity QGT, (c) velocity ring 81D, (d) temperature PET, (e) temperature QGT, (f) temperature ring 81D.

stronger temperature signal. The center of the PE ring at 500 meters is 8°C, and inside the QG ring it is 11°C. A superposition of the PE temperature and velocity fields at 100 m on day 24 is shown in Fig. 16. The cold ring and near field circulation are visible in the velocity field, but because the near-field circulation is barotropic only the ring has a strong temperature signal. The remainder of the warm outbreak can be seen to the west of the cold ring. Similar patterns have been observed in maps of SST shortly after the formation of a new cold ring. The direction and approximate strength of the near-field circulation found here was also observed in sea surface height measurements adjacent to a newly formed cold ring (Glenn 1989).

Vertical sections taken through the cold rings are shown in Fig. 17 together with sections through ring BOB by Vastano et al. (1980) and Olson (1980). The stronger temperature dome in the PE ring is evident; the core temperature at 500 m compares well with ring BOB. The velocity in the PE ring is stronger near the surface and extends deeper into the water column than it does in the QG ring. The maximum velocity of 120 cm s^{-1} in the PE ring is in good agreement with observed cold rings but the QG ring is a little weak at 70 cm s^{-1}. The deep core velocity seen in the PE calculation is typical of cold core rings. Another noticeable difference in the sections is the presence of small scales throughout the PE fields which are almost completely absent in the QG sections.

6. QG adjusted initial condition: PET–QGI

In this section, the effect of using an initial condition for the PE model that was dynamically adjusted by the QG model is studied. The third day of the QG model simulation with bottom topography was used to derive the initial conditions for the PE model. After three days, the QG model has essentially completed the first phase of the three-phase adjustment process and begun the second phase. There are broad, slow barotropic re-

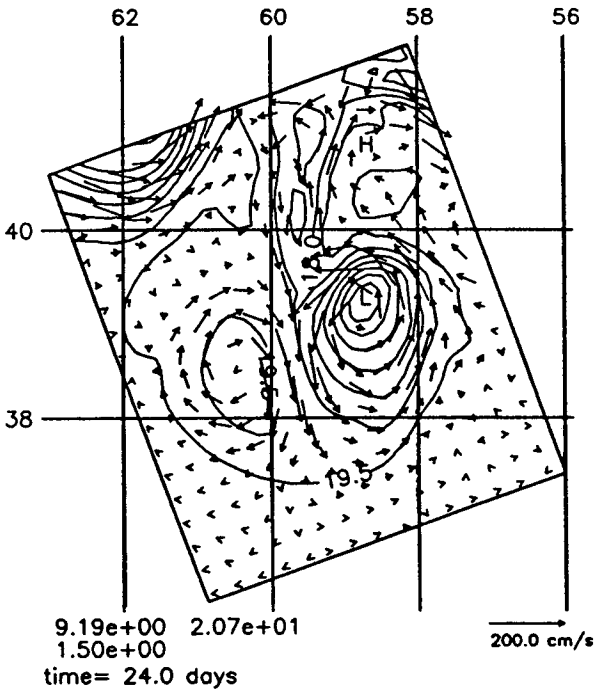

FIG. 16. PET: Cold ring, temperature and velocity at 100 meters.

circulations spun up in the regions adjacent to the stream, which are correlated with the shape and size of the initial meander pattern. When compared with the initial adjustment of the PE model, they are weaker and larger in horizontal extent. It was shown by Leith (1980) that quasi-geostrophy is the first level of the nonlinear normal model initialization used to project PE variables onto the slow manifold. The use of the QG model here is intended to be an approximation to this first level of normal mode initialization. These initial conditions used only the geostrophic velocity derived from the QG model streamfunction and did not include the horizontal divergence in the initial condition. As a result, the initial fields are only an approximation to the normal-mode initialization discussed by Leith, but it is hoped that they will result in a smoother evolution in the PE model than the analytic feature model initialization.

Because most of the evolution of the stream is similar to run PET, only the final temperature at 300 m is shown in Fig. 18. The early evolution is smoother in this calculation than that initialized with the analytic feature model, but the general characteristics are the same. The troughs are not as deep and the stream has less small scale variability than run PET. The cold ring formation occurs about 4–5 days earlier while the warm ring formation is not strongly affected as a result of the adjusted initial condition. Both rings are smaller in size than for PET but they are still very realistic. The stream is smoother and there are fewer small scales present than when the PE model was initialized directly from the feature model. Most important is the reduction of the unrealistic large scale meander present at the end of run PET. The use of the QG model to dynamically adjust the initial condition of the PE calculation does affect the results on space and time scales of interest. The growth of the large meander after day 24 is at least partially related to errors in the initial condition. Additional experiments are needed to determine initialization techniques that will result in the best model integration.

7. PRE-EVA analysis

In this section, the PRE-EVA package will be applied to the study of the warm and cold ring formation events discussed in section 5c. The region of analysis has been concentrated on the location of early development of the meander's pinchoff of the meander neck. The dominant terms in each ring formation process is examined in terms of a time series of horizontal maps in the appropriate subregion of interest. In section 7a, the formation of C_2 in experiment PET is studied. In section 7b, the formation of warm ring W_5 produced in the same experiment is investigated.

a. Cold ring formation

In this section, the formation of ring C_2 will be studied with the PRE-EVA analysis package. The subregion in which the horizontal maps have been calculated is shown in Fig. 19.

Selected terms from the vorticity equation at 300 m are shown in Figs. 20a–e. All other terms in Eq. (19) are negligible in the vorticity balance and will not be shown. The streamfunction is presented in the upper left for reference to the stream and ring positions. The deepening meander is evident on day 8 in the $\dot{R}$ term as the vorticity along the edge of the stream is moving to the south. The primary source is $\Delta_0 F_R$ with smaller contributions from fD, and $\Delta_1 F_R$. The ageostrophic advection ($\Delta_1 F_R$) and divergence terms (fD) are acting to slow the growth of the developing meander. Here fD is providing some of the vorticity that is being redistributed in the horizontal by the geostrophic advection term ($\Delta_0 F_R$).

On day 12, Fig. 20b, the core of the deepening meander is seen as a positive patch in the upper central part of the vorticity field. The meander is being advected to the south and east by $\Delta_0 F_R$ and slowed slightly by $\Delta_1 F_R$. The meander is also beginning to interact with the existing cold ring C_1. The quasi-geostrophic stretching term remains important and the filtering activity is small in the region of the forming meander.

Two days later, Fig. 20c, the meander has deepened considerably and the vorticity front stretches from north to south through the middle of the region. The forming neck is visible in the streamfunction field at

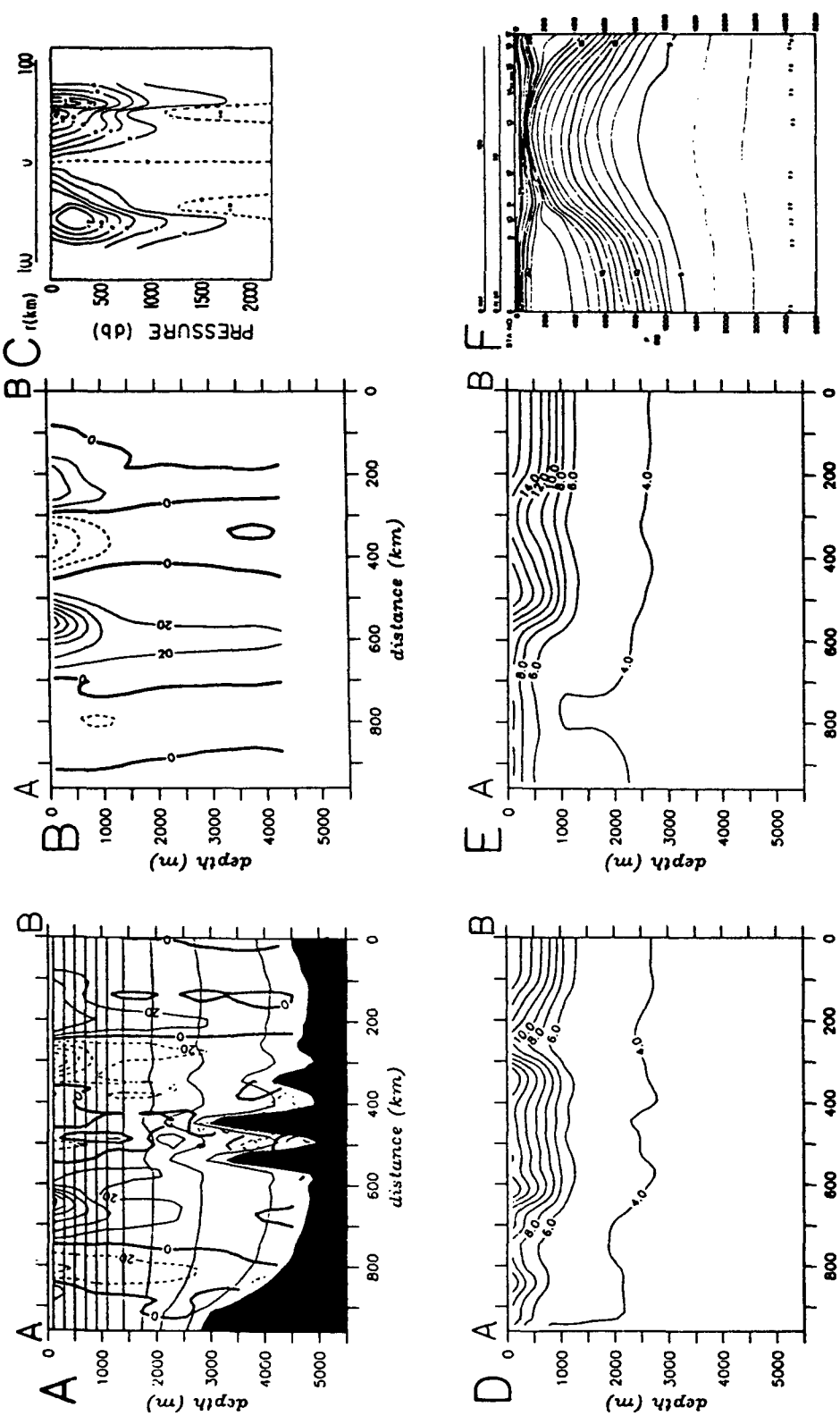

FIG. 17. Vertical sections: (a) velocity PET, (b) velocity QGT, (c) velocity ring BOB, (d) temperature PET, (e) temperature QGT, (f) temperature ring BOB.

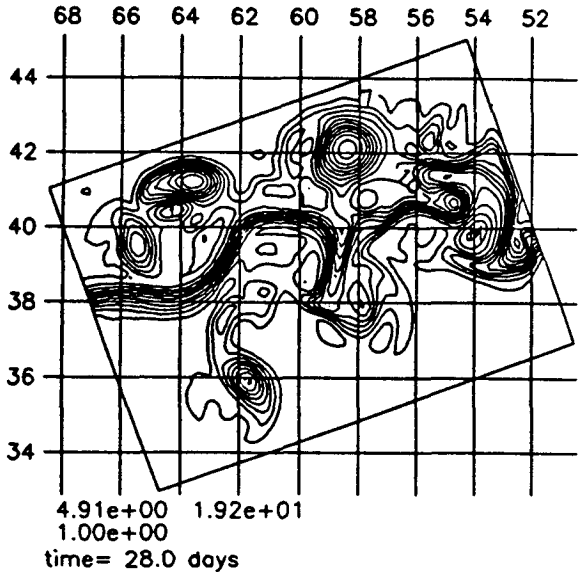

FIG. 18. PET_QGI: Temperature at 300 meters on day 28.

location 1. The vorticity along the western edge of the meander is decreasing due to $\Delta_0 F_R$ and $\Delta_1 F_R$. It is these horizontal advections that are causing the neck to pinch off in the vorticity field. At this time, the ageostrophic term is acting together with the geostrophic term to accelerate the ring cutoff but at the base of the meander $\Delta_0 F_R$ and $\Delta_1 F_R$ have the opposite sign. The horizontal filter is not negligible in the overall balance but only removes vorticity, which is cascading to small scales.

On day 18, Fig. 20d, the neck has just pinched off in R, and the main core of the stream is moving back to the north by $\Delta_0 F_R$. There is very little activity where the neck has already pinched off. On day 24, Fig. 20e, the cold ring has completely separated from the stream and is visible as a patch of positive vorticity in the southern part of the subregion.

The available gravitational energy balances at 300 m are shown in Figs. 21a–e. The center of the jet is the region of minimum A and the slope and Sargasso waters are regions of large A. On day 8, Fig. 21a, the negative $\dot{A}$ term along the leading edge of the meander trough indicates that the jet core is moving to the southeast. $\Delta_0 F_A$ is advecting A into the region while the ageostrophic term δf_A works against it in the upper (location 1) and lower (location 2) meander regions. b is converting A to K in the upper meander and along the eastern edge of the meander (location 3) but is increasing A at the base of the deepening trough (location 2).

On day 12, Fig. 21b, the dominant balance is between $\Delta_0 F_A$, δf_A, and b with smaller contributions from $\Delta_1 F_A$. Geostrophic advections are importing A from the west into the developing meander as indicated by the positive contribution at location 1. The ageostrophic horizontal advection is importing A in the upper meander where it is exported vertically by δf_A. b is converting A to K along the western side of the deepening meander, locations 1, while it is accumulating A at the base of the meander, location 2. Horizontal advections continue to decrease A in the region of the closing neck and increase A in the developing cold ring.

Two days later, Fig. 21c, the pinching neck is visible in the streamfunction field. The pinchoff is still occurring primarily along the western side of the meander by $\Delta_0 F_A$, δf_A, and b. Baroclinic conversions are continuing to accelerate the jet at location 1 and accumulate A at the base of the meander, location 2.

By day 18, Fig. 21d, there is very little activity in the center of the region. The ring is separating in A and is being advected to the south by $\Delta_0 F_A$. Along the border between the new cold ring and the near-field anticyclone, location 1, there is a continued conversion of A to K via buoyancy work. The source of this potential energy is due to both horizontal and vertical advection. This acceleration of the dipole jet continues for two more days as the pair moves to the south. On day 24, the cold ring has separated from the stream in A; only a weak filament remains where the neck has pinched off. The acceleration of the dipole jet has stopped and the ring is almost stationary.

The horizontal divergence and kinetic energy equations were also calculated at 300 m. In the divergence equation, the geostrophic balance between $D_2 P$ and fR was dominant throughout the simulation. There was a small contribution in the newly formed cold ring from the nonlinear balance term $\Delta_0 \Delta_0$ but it was not important in the ring formation process. The kinetic energy equation showed an acceleration of the meander jet primarily due to horizontal advection and pressure

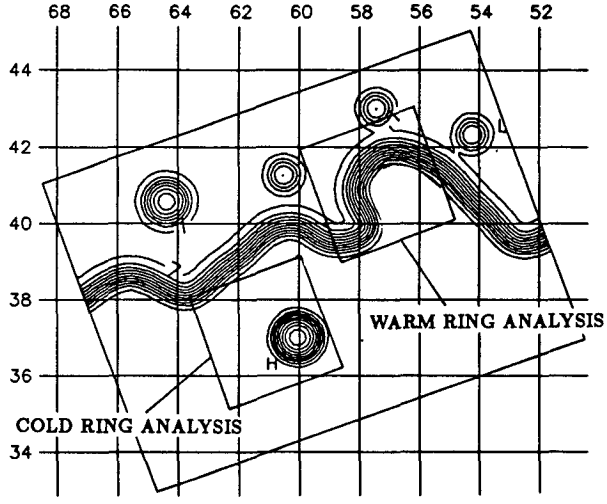

FIG. 19. Regions of PRE-EVA analysis, cold and warm ring studies.

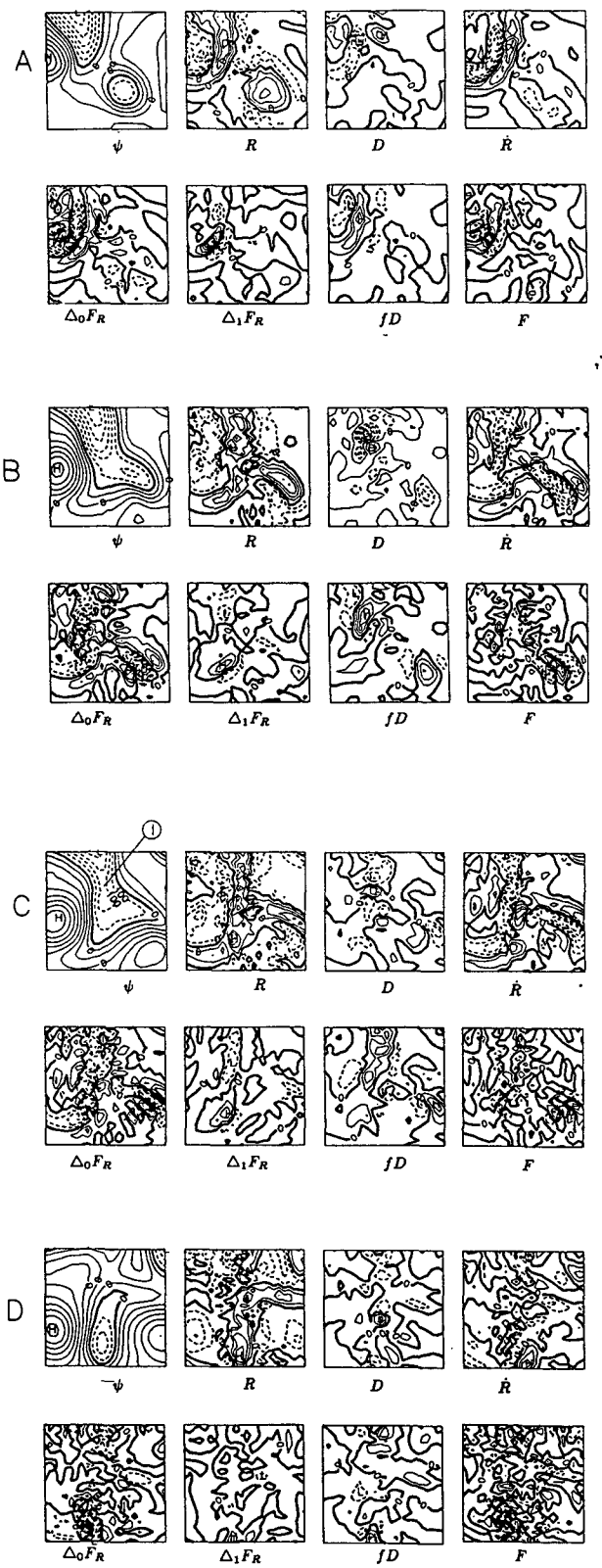

FIG. 20. PRE-EVA analysis: Cold ring vorticity balances at (a) day 8, (b) day 12, (c) day 14, (d) day 18, (e) day 24.

FIG. 20. (*Continued*)

work. These terms did not add to the conclusions drawn from the previous analysis.

A schematic, which summarizes the cold ring formation process, is given in Fig. 22. There are two phases of the ring formation, meander growth and pinchoff of the neck. The meander growth phase occurs between days 8 and 13. During this time, the meander vorticity is developing to the south and east by geostrophic advection and slowed by ageostrophic horizontal advection and horizontal divergence. A is imported to the southeast by horizontal advection and exported to the deeper levels by vertical advection. Buoyancy conversions are accumulating A at the base of the meander and converting A to K along the western side of the deepening meander. Between days 13 and 15 the final ring pinchoff occurs. In the neck region, the vorticity is separated from the stream by both geostrophic and ageostrophic advection from the west and slowed by the horizontal divergence term. The available gravitational energy in the core of the ring is increased by horizontal advection from the pinching neck. Along the western side of the meander jet, A is imported by vertical advection and converted to K via b. At the base of the meander, baroclinic conversion is increasing A and vertical advection is exporting some of this energy to the deeper levels. After the ring has separated, the baroclinic conversion from the near-field circulation continues to accelerate the ring by importing A in the vertical and converting to K via b. It is believed that the accumulations of A and R by ageostrophic horizontal and vertical terms are responsible for the increased strength and temperature signal of the new PE ring when compared to the new QG ring.

The PRE-EVA analysis package was also applied to the cold ring formation in run PEF. This was done to determine why the cold ring did not form as cleanly without bottom topography. The early stages of ring formation are almost identical between the two calculations. The meander growth period, acceleration of the western side of the deepening meander, and accumulation of A at the base of the meander are all observed. The difference occurs after the growth phase

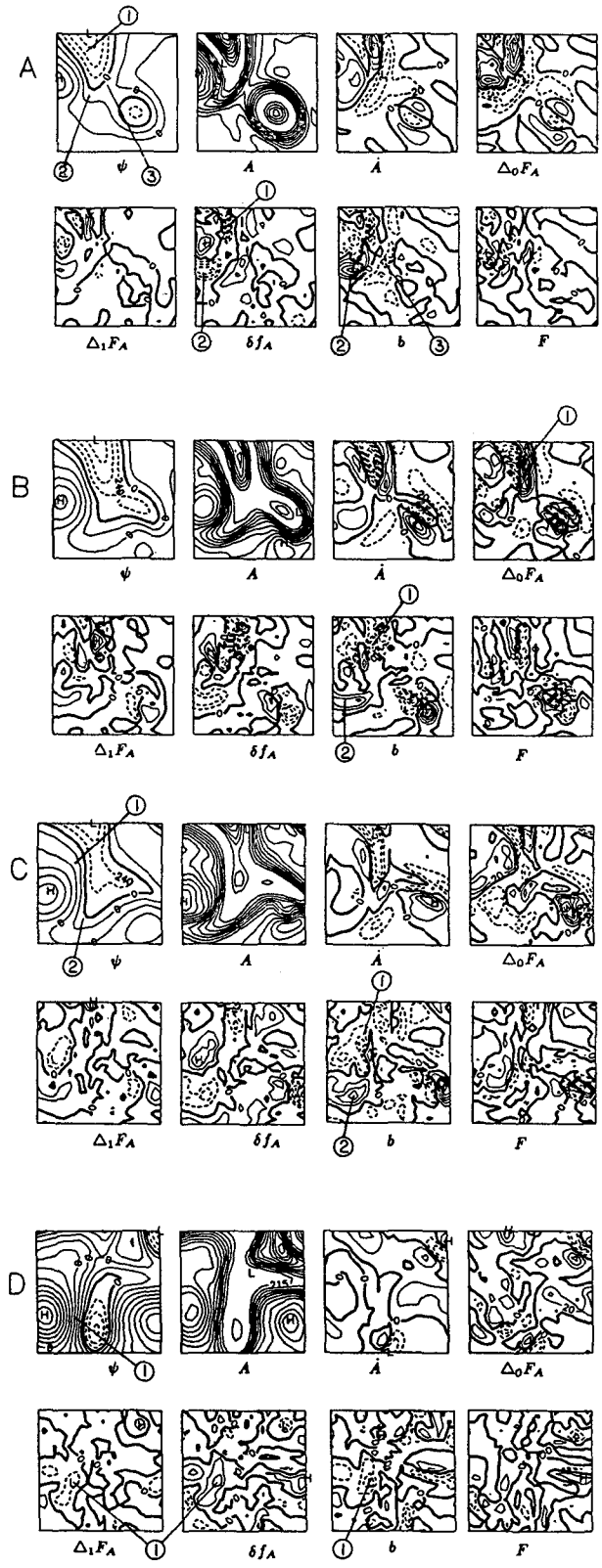

FIG. 21. PRE-EVA analysis: Cold ring available gravitational energy balances at (a) day 8, (b) day 12, (c) day 14, (d) day 18, (e) day 24.

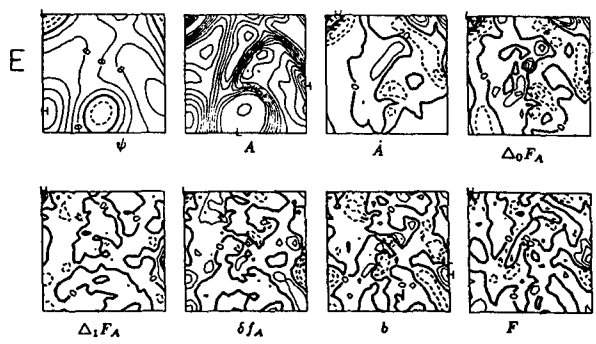

FIG. 21. (*Continued*)

when the neck begins to pinch off. As discussed earlier in this section, the cutoff in PET was achieved by geostrophic and ageostrophic advection from the western side of the deepened meander. Without bottom topography, this advection from the west still occurs, but now the eastern side of the meander is also advected towards the east. As a result, the neck does not separate completely but also shifts to the east. The cold ring

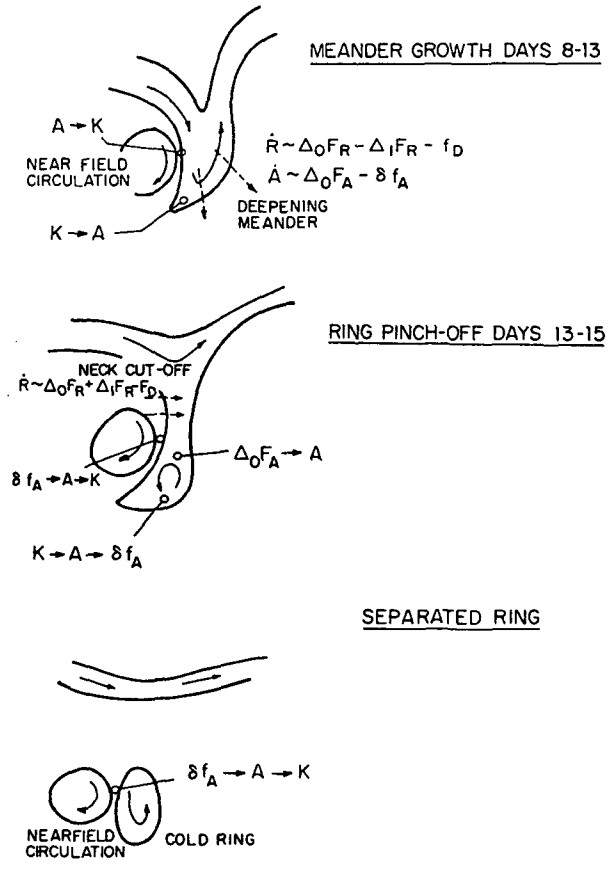

FIG. 22. Schematic of cold ring formation process.

formation took place directly over the New England Seamounts. It is believed that the addition of topography has acted to block the eastward movement of the stream during the final ring cutoff. The presence of topography has facilitated the ring formation in this case but, in general, it is not believed to be necessary for the cold ring formation process.

The dynamical processes of the cold ring formation event discussed here are similar to, but contain important differences from, the quasi-geostrophic cold ring formation analyzed with EVA by RSP. The early meander development by geostrophic advections of relative vorticity are found in both studies but the additional ageostrophic advections included in the primitive equations were seen to affect the ring formation in several ways. $\Delta_1 F_R$ acts to slow meander growth, accumulate R in the developing cold ring and, once the meander has deepened, these ageostrophic advections accelerate the final cutoff of vorticity at the neck. The nonlinear local cascade of R at the pinching neck and elimination of small scales by F found in the quasi-geostrophic study is not seen here. It appears that, although this filtering activity was important to the final ring formation in the QG analysis, it is not critical to the process of ring formation in the primitive equation model. The acceleration of the western meander jet and the accumulation of A in the forming ring due to baroclinic conversions is found in both models, but the processes are stronger and are found only along the upstream side of the meander in the primitive equation model. The ageostrophic vertical advection is responsible for slowing the early meander growth and exporting A vertically in the core of the developing ring. The baroclinic conversion continues to accelerate the cold ring after formation in the primitive equation model but is present only during the meander deepening phase of the quasi-geostrophic model. These differences are responsible for the more realistic ring formation produced by the primitive equation model. The ageostrophic terms have acted to slow the meander growth and delay the ring formation by several days. The increased baroclinic conversion and additional ageostrophic terms contributed to the more realistic baroclinicity and stronger velocities in the primitive equation ring but the first-order processes of meander growth and ring formation were represented in the QG study of RSP.

b. *Warm ring formation event*

In this section, the PRE-EVA analysis package will be applied to the warm ring formation event in experiment PET. The region of analysis is indicated in Fig. 19. A time series of horizontal maps has been calculated. The dominant terms are shown on the days which are necessary to fully describe the ring formation process; all of the terms not shown are negligible in the overall balances. In each case the streamfunction has been included in the upper left for reference.

The relative vorticity equation terms at 300 m are shown in Fig. 23. On day 6, Fig. 23a, the northward meander and developing upstream trough can be seen in the streamfunction field. The vorticity is made up of elongated patches running along the stream, positive on the slope side and negative on the Sargasso side. The time rate of change indicates that the meander is growing to the north in the central part of the meander (location 1) and to the south along the eastern side (location 2). The wave pattern in $\dot{R}$ at location 3 indicates that the trough just upstream of the northward meander is moving to the east. The primary term responsible for these changes is $\Delta_0 F_R$ with small fD working against it. The patch of negative vorticity along the western meander (location 4) is being advected into the growing meander by the geostrophic velocity; see the $\Delta_0 F_R$ term.

Three days later, Fig. 23b, the meander has developed a large patch of negative vorticity at location 4 and has elongated as was indicated by the previous tendencies. The trough at location 3 is continuing to be advected to the east by $\Delta_0 F_R$. On the eastern side of the meander (location 2), $\dot{R}$ indicates that the neck is continuing to form by horizontal advection ($\Delta_0 F_R$) and horizontal divergence (fD). The filter is removing small scales generated by horizontal advection along the stream meander.

On day 12, Fig. 23c, the pinching neck can be seen in both the streamfunction and vorticity fields. The neck formation is due to the eastward moving upstream trough (location 3), and the deepening of the meander at location 2. The trough movement is dominated by geostrophic advection, but the meander development in the east is a balance of $\Delta_0 F_R$ and fD.

By day 15, Fig. 23d, the negative patch of vorticity in the core of the ring has almost completely separated from the stream. $\Delta_1 F_R$ is large along the northwestern portion of the newly formed ring, location 5. This is where the large patch of water was shed from the newly formed ring discussed in section 5c. This indicates that it is the cross-isobar flow which was responsible for the loss of water from the new ring. The ageostrophic advection is large in this region only while the water is being advected from the warm ring. To the south, the remainder of the trough can be seen moving downstream just past the pinching neck, location 3. The vorticity completely separates from the stream on day 18; day 24 is shown here for comparison with the available gravitational energy terms.

The available gravitational energy terms at 300 m are shown in Fig. 24. The core of the Gulf Stream jet is characterized by a low in A, and the slope and Sargasso waters are a region of large A. The shingle-like feature discussed in section 5c is also visible in the A map. As can be seen in the $\dot{A}$ term on day 6, Fig. 24a,

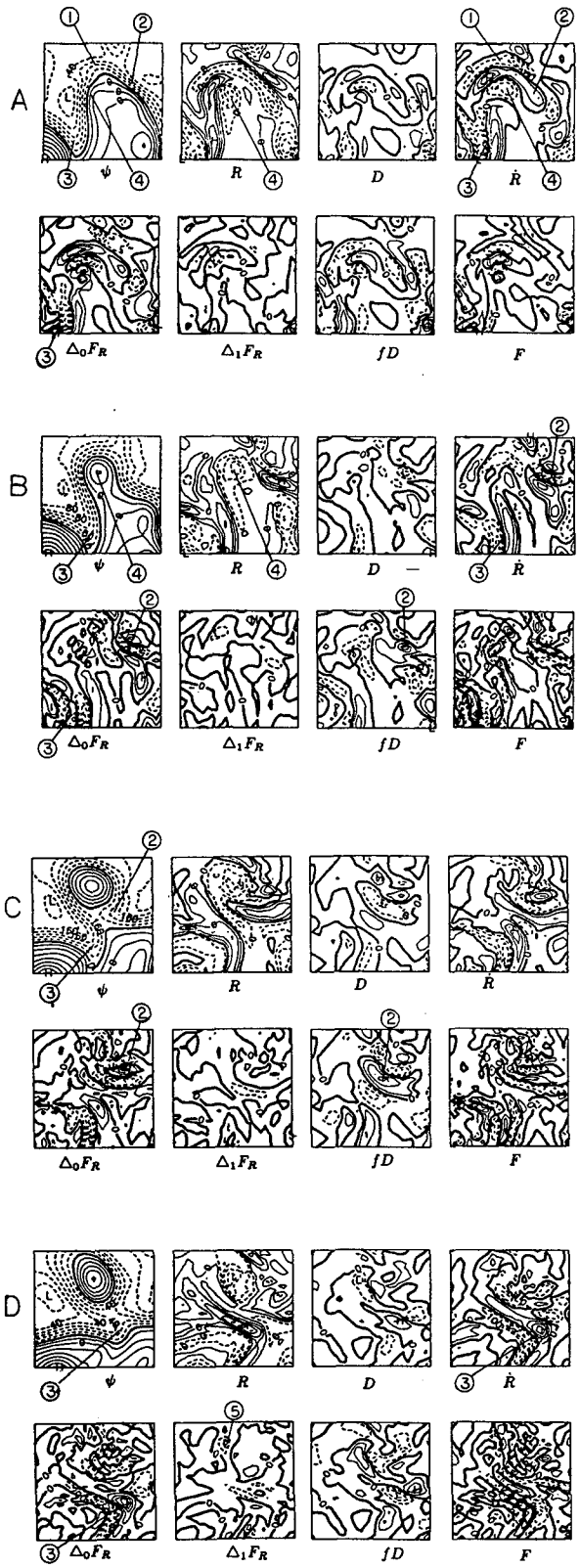

FIG. 23. PRE-EVA analysis: Warm ring vorticity balances at (a) day 6, (b) day 9, (c) day 12, (d) day 15, (e) day 24.

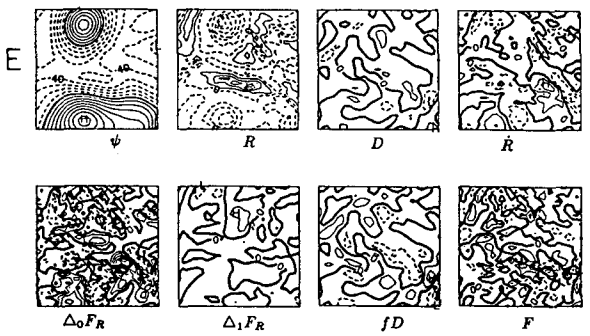

FIG. 23. (*Continued*)

the meander is moving to the north at location 1 and the upstream trough is moving to the east in location 3. As in the vorticity equation, the dominant term is the geostrophic advection ($\Delta_0 F_A$) with smaller contributions from δf_A.

Three days later, the meander has taken on an elongated looping shape, the upstream trough is moving to the east (location 3) and the neck is forming along the eastern side of the meander (location 2). The pinching neck is predominantly due to $\Delta_0 F_A$ but some of this A is exported vertically by δf_A and converted to K by b. Ageostrophic horizontal advection is also increasing the rate of neck formation. There is an accumulation of A in the core of the forming ring due to geostrophic advection.

On day 12, Fig. 24c, the neck is beginning to close, horizontal advection is moving the upstream trough to the east and the downstream trough to the south. Baroclinic conversion is generating A along the southern edge of the forming ring (location 4) where it is advected into the core of the developing ring by $\Delta_0 F_A$. At this time, A is still increasing in the ring core.

Three days later, Fig. 24d, there is very little activity in the vicinity of the pinching ring. The high in A has just about separated from the stream and the meander trough is moving downstream. On day 24 the warm ring has separated from the stream and is moving slowly to the northwest.

A schematic, which summarizes the processes in the warm ring formation event, is shown in Fig. 25. The process is characterized by two phases, meander growth and neck pinchoff. The meander growth takes place between days 6 and 12. During this time, the meander becomes elongated and begins the neck formation. The meander grows to the north by horizontal advections of R and A, and there is a net accumulation of R and A in the ring core by advection from upstream. The neck formation is caused by the eastward propagation of the upstream trough and the westward movement of the eastern side of the meander. Geostrophic advection is responsible for the trough propagation, but both horizontal and vertical processes are active where

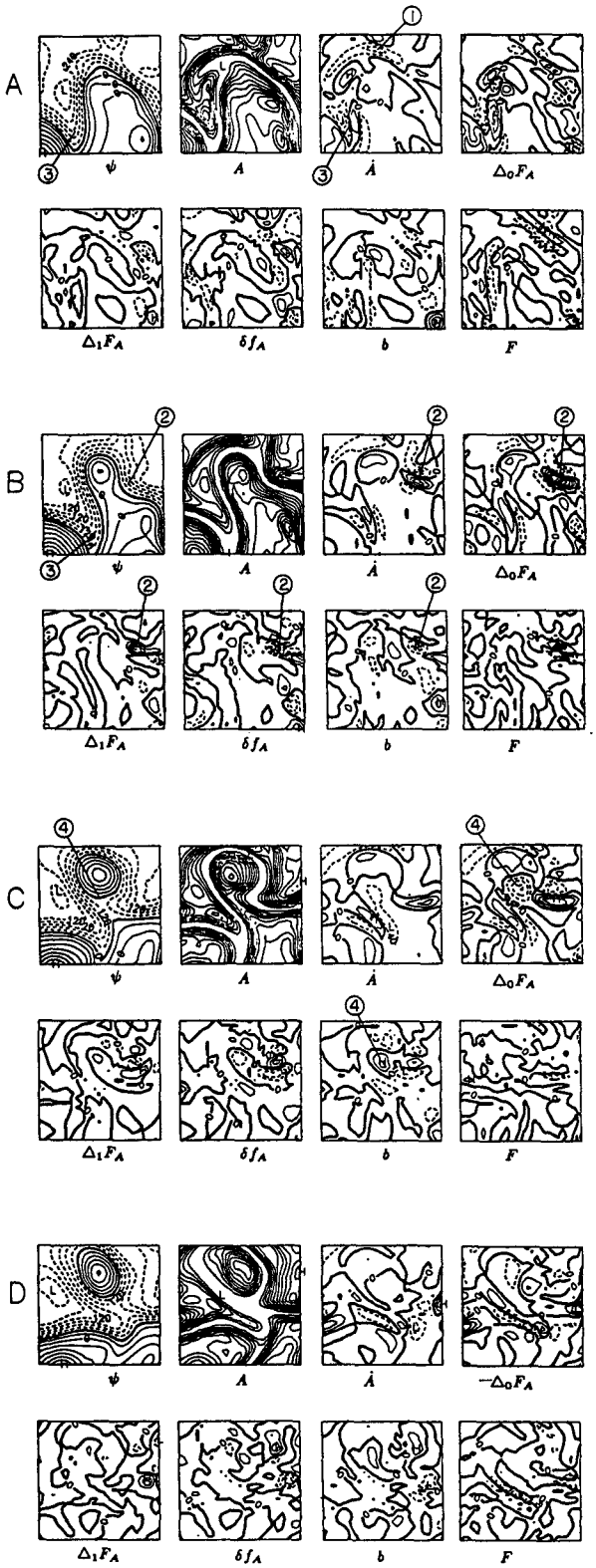

FIG. 24. PRE-EVA analysis: Warm ring available gravitational energy balances at (a) day 6, (b) day 9, (c) day 12, (d) day 15, (e) day 24.

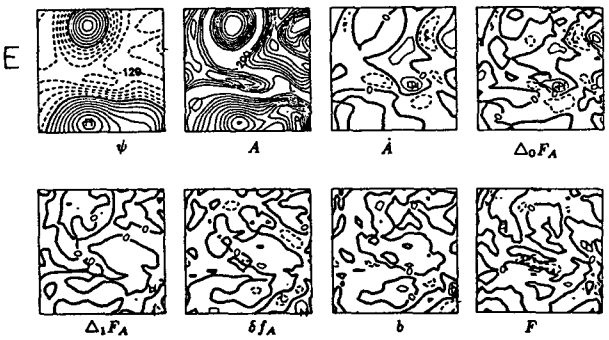

FIG. 24. (*Continued*)

the neck is forming in the east. During the second phase, K is being converted to A by b at the southern edge of the ring and advected into the core of the ring by $\Delta_0 F_A$. It is not believed that this final conversion of K to A is necessary for ring formation but it does increase the baroclinic signature of the new ring. Ageostrophic horizontal advection is responsible for a loss of water from the new ring to the northwest.

The process of warm ring formation described here is quite similar to that found using EVA in the quasi-geostrophic studies of RSP. The early development of the meander is dominated by horizontal processes in both models; however, the initial growth period is more rapid and distinct in the QG model. The formation and cutoff of the neck due to the eastward propagation of the upstream trough is common to both studies. There are two distinct differences in the primitive equation ring formation. In addition to the neck development from the west by the upstream trough, the neck region also closes from the eastern side due to horizontal and vertical advections and baroclinic conversion. This activity is seen to accelerate the ring formation process. The center of the primitive equation warm ring has a stronger baroclinic structure and increased vorticity due to horizontal advections and a baroclinic conversion at the neck late in the ring formation. Although these differences are responsible for a stronger and more realistic warm ring in the primitive equation model, the essential process of warm ring formation was captured by the quasi-geostrophic model in RSP.

8. Summary and conclusions

Satellite IR data from a four week period between 23 November and 19 December 1984 was used as the basis for model initialization and verification. During this period many dynamical events occurred: new cold and warm rings were formed, warm rings interacted with and were absorbed by the Gulf Stream, and meander systems evolved. The feature model used in this study was based on the Pegasus dataset and had a

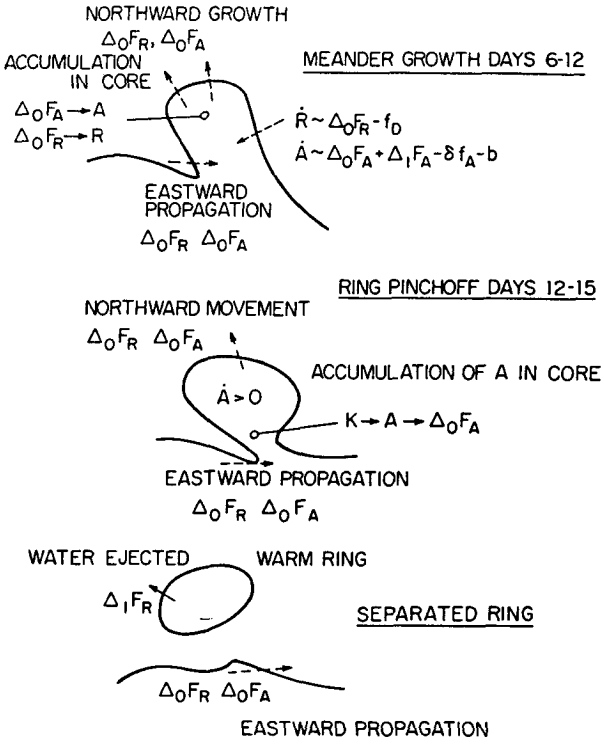

FIG. 25. Schematic of warm ring formation process.

maximum velocity of 165 cm s^{-1} at the surface, 25 cm s^{-1} at 1000 m, and 5 cm s^{-1} at 4500 m. Ten levels were used in the vertical and the horizontal grid spacing was 15 km.

Both the PE and QG models reproduced the major dynamical events in good agreement with the available SST data. A schematic representation of the final state of the NOAA analysis, PET, and QGT are shown in Figs. 26a–c. The location and number of rings present in the calculations agree reasonably well. Both calculations produced an extra cold ring near 37.5°N, 57°W, which is not observed in the satellite data. The warm ring near 42°N, 61°W is labeled as $W_{2,6}$ in Fig. 26a because it is unclear from the observations if W_2 interacted with the stream and then separated or was absorbed and a new warm ring formed. The corresponding ring in the model calculations is labeled as W_6 because it is a newly formed ring. The final stream position in the QG fields compared well with the NOAA analysis; however, the large meander west of 60°W in the PE fields is evident in Fig. 26c.

The deep velocity fields showed some interesting differences due to both model physics and addition of bottom topography. The flat bottom fields were dominated by large, basin-scale circulations in both the PE and QG calculations. The addition of bottom topography broke down the basin-scale circulations and introduced energetic jets and eddies associated with the horizontal scale of the bottom topography, 50 to 200 km in both models. Both PE calculations were energetic below 50 km but the QG calculations contained no energy at these small scales. The deep velocity fields were stronger at scales less than 200 km in the PE model than in the QG model, regardless of topography.

The implementation of steep and tall bottom topography in the QG model resulted in a steering of the flow fields and generation of local jets around the topographic features. This steering is accomplished through the stretching of potential vorticity alone. Calculation of the vertical velocity at the bottom indicated that additional vertical advection terms, which are neglected in the quasi-geostrophic approximation, were larger than order Rossby number at approximately 5% of the grid points, primarily in the vicinity of the New England Seamounts. It is concluded that, in this case, the topographic steering in the QG model is consistent with what is found in the more complete primitive equation model but that important physics are neglected. If quasi-geostrophic models are applied to problems with steep and tall topography, the vertical velocity at the bottom should be monitored in order to estimate the magnitude of the neglected terms.

The QG model was used to dynamically adjust the analytic feature models for initialization of the PE model. As a result, the large meandering of the stream was reduced to be in better agreement with the observations. The final state of this calculation is shown in Fig. 26d. It is concluded that using quasi-geostrophic

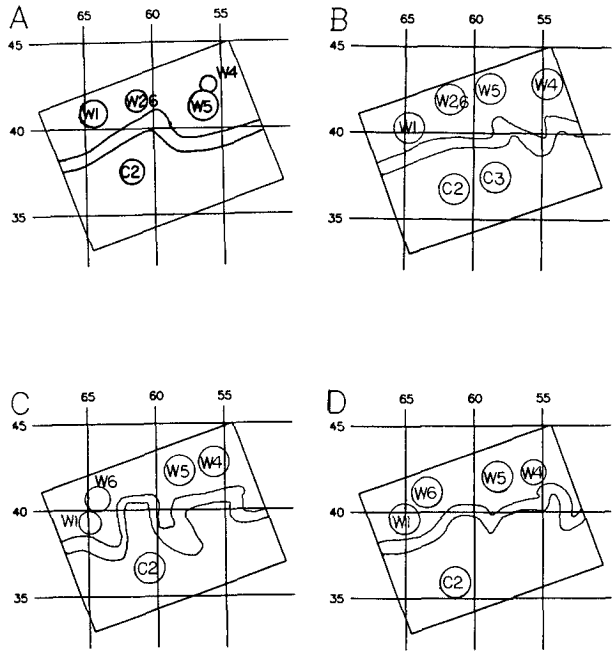

FIG. 26. Schematic of final state in (a) NOAA analysis, (b) QGT, (c) PET, (d) PET_QGI.

dynamics to adjust the initial conditions for the PE model has improved the PE simulation. It is believed that the development of the large meander in the PE model is, at least partially, a result of errors in the initial condition. The fact that it is not observed until day 24 is an indication of the growth rate of such errors. Further studies are needed to determine if this is a characteristic of the primitive equations in general or dependent on this specific case study. If similar growth rates are found for a variety of initial conditions and model domains, better initialization techniques will have to be developed in order to obtain accurate and meaningful PE calculations beyond one month in duration.

The PRE-EVA analysis package was applied to the study of the cold and warm ring formation events. The cold ring formation is preceded by a period of meander growth due to geostrophic and ageostrophic advection. Baroclinic conversion increased A in the forming ring and increased K along the west side of the meander jet. The final ring pinchoff was accomplished by geostrophic and ageostrophic horizontal advection of vorticity from the west side of the deepening meander. The baroclinic processes continue to develop and accelerate the ring after separation. The warm ring formation also undergoes growth and pinchoff phases. During the growth phase, horizontal advection extends the meander to the north and accumulates R and A in the ring core. Neck formation is due to the eastward propagation of the upstream trough and pinching of the neck from the eastern side of the meander. At the final pinchoff baroclinic conversion and horizontal advection increase A in the ring core as the trough propagates to the east and separates the ring from the stream. The basic processes of the cold and warm ring formation events described here are in general agreement with the quasi-geostrophic study done by RSP. The more realistic rings produced by the PE model were attributed to the additional horizontal and vertical advection terms included in primitive equation physics.

The basic processes of the warm and cold ring formation events in this case study were seen to be quite different. Based on the analysis in this paper, there is no reason to believe that each of these processes could not be responsible for forming a ring of opposite circulation, subject to the right initial conditions. An interesting topic of future study is to investigate the generality of these ring formation mechanisms for warm and cold rings by initializing the model with a stream axis flipped in the meridional direction.

The results in this paper indicate that both the primitive equation and quasi-geostrophic models can play an important role in the simulation of Gulf Stream meanders and ring formation events. The primitive equation model is appropriate for detailed and definitive studies of meander and ring formation processes because it contains more complete physics. Further intercomparison of PE and QG model results will establish the regional space–time and phenomenological domain of QG reliability. Both models are believed to be comparable for the simulation of major evolutionary events on time scales of less than three weeks. It is desirable to use the primitive equation model for longer integrations because the primitive equation physics and interaction with bottom topography may become important to the large-scale upper thermocline evolution on these time scales. However, the results in this paper indicate that the long time behavior of the primitive equation model is sensitive to the initialization procedure and that small changes in the initial conditions can eventually result in large changes in the model fields. Dynamically adjusting the initial conditions is a very important area of research and needs to be studied further. Computational resources must also be considered in the selection of the most appropriate model. For the simulations in this paper, the two models required similar CPU time on a vector processing machine but the quasi-geostrophic model is approximately a factor of 10 faster on a scalar machine.

Acknowledgments. We are grateful to Dr. Nadia Pinardi for her input to the energy and vorticity analysis of the warm and cold ring formation events. The anonymous reviewers are also thanked for their constructive and valuable suggestions. This work was supported by the Office of Naval Research under Contract N00014-84-C-0461 to Harvard University.

REFERENCES

Adamec, D., 1988: Numerical simulations of the effects of seamounts and vertical resolution on strong ocean flows. *J. Phys. Oceanogr.*, **18,** 258–269.

Batteen, M. L., 1984: Numerical studies of mesoscale eddies using quasi-geostrophic and primitive equation ocean models. PhD thesis, Oregon State University.

Beckmann, A., 1989: private communication.

Bower, A. S., H. T. Rossby and J. L. Lillibridge, 1985: The Gulf Stream—barrier or blender? *J. Phys. Oceanogr.*, **15,** 24–32.

Charney, J. G., R. Fjortoft and J. Von Neumann, 1950: Numerical integration of the barotropic vorticity equation. *Tellus,* **2,** 237–254.

Cornillon, P., D. Evans and W. Large, 1986: Warm outbreaks of the Gulf Stream into the Sargasso Sea. *J. Geophys. Res.*, **91,** 6583–6596.

Gent, P. R., and J. C. McWilliams, 1983: Regimes of validity for balanced models. *Dyn. Atmos. Oceans,* **7,** 167–183.

Gill, A. E., 1982: *Atmosphere-Ocean Dynamics.* Academic.

Glenn, S. M., 1989: private communication.

Haidvogel, D. B., 1983: Periodic and regional models. *Eddies in Marine Science,* A. R. Robinson, Ed., 404–437.

Hurlburt, H. E., and J. D. Thompson, 1984: Preliminary results from a numerical study of the New England Seamount chain influence on the Gulf Stream. *Predictability of Fluid Motions,* G. Holloway, B. J. West, Eds. Amer. Inst. Phys., 489–504.

Ikeda, M., 1981: Meanders and detached eddies of a strong eastward flowing jet using a two layer quasi-geostrophic model. *J. Phys. Oceanogr.*, **11,** 526–540.

——, and J. R. Apel, 1981: Mesoscale eddies detached from spatially growing meanders in an eastward flowing oceanic jet using a two layer quasi-geostrophic model. *J. Phys. Oceanogr.*, **11,** 1638–1661.

Joyce, T. M., 1984: Velocity and hydrographic structure of a Gulf Stream warm core ring. *J. Phys. Oceanogr.*, **14,** 936–947.

Large, W. C., J. C. McWilliams and P. P. Niiler, 1986: Upper ocean thermal response to strong autumnal forcing of the northeast Pacific. *J. Phys. Oceanogr.*, **16,** 1524–1550.

Leith, C., 1980: Nonlinear normal mode initialization and quasi-geostrophic theory. *J. Atmos. Sci.*, **37,** 958–968.

Lorenz, E. N., 1960: Energy and numerical weather prediction. *J. Atmos. Sci.*, **19,** 39–51.

McHugh, P., and J. Clark, 1984: Oceanographic analysis of the Gulf Stream region. *Ocean. Monthly Summary,* **4,** 11–12.

Miller, N., A. R. Robinson and D. B. Haidvogel, 1981: A baroclinic open ocean model. *J. Comput. Phys.*, **50,** 38–70.

Niiler, P. P., and A. R. Robinson, 1967: The theory of free inertial jets. Part II: A numerical experiment for the path of the Gulf Stream, *Tellus,* **19,** 601–619.

Olson, D. B., 1980: The physical oceanography of two rings observed by the cyclonic ring experiment. Part II: Dynamics. *J. Phys. Oceanogr.*, **10,** 514–528.

Pratt, L. J., and M. E. Stern, 1986: Dynamics of potential vorticity fronts and eddy detachment. *J. Phys. Oceanogr.*, **16,** 1101–1120.

Rhines, P. B., 1977: The dynamics of unsteady currents. *Marine Modelling, The Sea,* Vol. 6, E. D. Goldberg, I. N. McCane, J. J. Obrien and H. H. Steele, Eds., 130 pp.

Robinson, A. R., and Leonard J. Walstad, 1987: The Harvard open ocean model: Calibration and application to dynamical process, forecasting, and data assimilation studies. *Appl. Numer. Math.*, **3,** 89–131.

——, M. A. Spall and N. Pinardi, 1988: Gulf Stream simulations and the dynamics of ring and meander processes. *J. Phys. Oceanogr.*, **18,** 1811–1853.

Shapiro, R., 1970: Smoothing, filtering, and boundary effects. *Rev. Geophys. Space Phys.*, **8,** 359–387.

Spall, M. A., 1989: Regional primitive equation modeling and analysis of the polymode data set. *Dyn. Atmos. Ocean.*, **14,** 125–174.

——, and A. R. Robinson, 1989: A new open ocean, hybrid coordinate primitive equation model. *Math. and Comp. in Sim.*, **31,** 241–269.

Vastano, A. C., J. E. Schmita and D. E. Hagan, 1980: The physical oceanography of two rings observed by the cyclonic ring experiment. Part I: Physical structures, *J. Phys. Oceanogr.*, **10,** 493–513.